Modelling and Navigation of Autonomous Vehicles on Roundabouts

by

Dave Mandyam

A thesis
presented to the University of Waterloo
in fulfillment of the
thesis requirement for the degree of
Master of Applied Science
in
Systems Design Engineering

Waterloo, Ontario, Canada, 2021

AUTHOR'S DECLARATION

I hereby declare that I am the sole author of this thesis. This is a true copy of the thesis, including any required final revisions, as accepted by my examiners.

I understand that my thesis may be made electronically available to the public.

Abstract

A path following controller was proposed that allows autonomous vehicles to safely navigate roundabouts. The controller consisted of a vector field algorithm that generated velocity commands to direct a vehicle. These velocity commands were fulfilled by an actuator controller that converts the velocity commands into wheel torques and steering angles that physically move a vehicle. This conversion is accomplished using an online optimization process that relies on an internal vehicle model to solve for necessary wheel torques and steering angles.

To test the controller's performance, a 16 degree of freedom vehicle dynamic model was developed with consideration for vehicle turn physics. Firstly, tire force data was gathered by performing driving maneuvers on a test track using a vehicle fitted with tire measurement equipment. The generated tire force data was used to compare various combined slip tire force models for their accuracy. The most accurate model was added to the high-fidelity vehicle model. Next, suspension kinematic data was generated using a simple testing procedure. The vehicle was equipped with the tire measurement equipment and the vehicle was raised a lowered with a hydraulic jack. Using displacement and orientation data from this test, a novel reduced order suspension kinematic model that reproduces the observed motion profile was developed.

Application of the path following controller to the high-fidelity model resulted in close following of a roundabout path with small deviations.

Acknowledgements

First and foremost, I would like to thank my supervisors, Dr. John McPhee and Dr. Nasser L. Azad. Without their support and guidance, I would not have been able to become the creative mind and thinker I aspired to be. Their patience and shrewdness were very inspiring to me and their encouraging attitudes helped me realize my potential.

I would also like to thank Dr. Ken Butts and the Toyota Technical Center for funding this project and for their wisdom. Dr Butts comments and technical expertise were valuable and motivating.

Special thanks to Dr Eihab Abdel-Rahman and Dr Christopher Nielsen for agreeing to review my thesis and for providing their meaningful feedback.

I am very grateful to Chris Shum and Matthew van Gennip for their assistance with vehicle instrumentation and data collection.

Lastly, I would like to thank my family for their unyielding support and everlasting love.

Dedication

I dedicate this work to my family.

Table of Contents

List of Figures

List of Tables

Chapter 1
Introduction

1.1 Autonomous Vehicles

Autonomous vehicles have gained popularity as a heading direction for future automobile designs. Developing autonomous vehicles requires addressing problems in planning, perception, and control [1]. These areas are oftentimes connected meaning knowledge in all three areas is necessary when developing autonomous vehicles. Commonly stated, there are five levels of autonomy used to characterize autonomous vehicles [2]. Higher levels of autonomy indicate greater functionality from vehicles and less interaction from drivers. Examples of level 1 autonomous vehicles are those with Advanced Driver Assisted Systems (ADAS) such as cruise controllers or anti-lock braking systems [3]. Recently, Tesla has achieved level 3 autonomy with their Autopilot system [4]. Under specific conditions, the Autopilot system allows Tesla vehicles to drive, park and turn autonomously.

Path planning is about generating reference paths for autonomous vehicles. These reference paths are designed to avoid collisions and to encourage vehicles to arrive at a desired destination. Popular approaches to path planning are those that can be combined with controllers or graph theoretic methods [5, 6]. Control theoretic approaches rely on potential fields can lead to smooth path generations however they do not guarantee arrival at destinations. On the other hand, graph theoretic algorithms offer flexibility by allowing weights to be assigned by direction. Paths that are feasible can be designed this way however graph theoretic approaches require discretizing motion spaces. This reduces path smoothness.

Perception deals with locating a vehicle and identifying its surroundings [1]. This is oftentimes accomplished using Light Detection and Ranging (LIDAR) sensory equipment, cameras or a fusion of perception elements to map a vehicle's environment. Combining these strategies with localization algorithms, estimates of a vehicle's position and the location of obstacles can be identified. Commonly, localization and mapping of vehicles are accomplished simultaneously. This is usually referred to a Simultaneous Localization and Mapping (SLAM).

SLAM techniques employ Bayesian filters, Kalman filters, or particle filters to accurately estimate position while scoping a surrounding environment.

Lastly, controllers actuate vehicles based on information from path planning algorithms [5]. Through combinations of feedback and feedforward controllers, commands can be delivered to vehicle accelerator pedals, brake pedals and the steering wheel to make the vehicle move appropriately. One of the most popular control methods is Model Predictive Control (MPC) [7]. An MPC relies on an internal vehicle model to compute control inputs that make a vehicle move in a desirable way. This is accomplished through an online optimization, with the internal vehicle model, such that an error function is reduced. A principal advantage of an MPC is the ability to handle constraints.

1.2 Roundabouts

Roundabouts are a roadway intersection type that were shown to lead to fewer vehicle collisions and pedestrian accidents compared to typical traffic stop intersections [8]. They can be identified by their distinct circular geometry. Roundabouts are considered safer than signalled intersections because they require slower vehicle speeds and greater driver vigilance. However, municipalities often choose not to construct roundabouts because of their expensive construction costs [9, 10]. Moreover, the slow vehicle speed requirement makes roundabouts ineffective for highway intersections with high speed limits. The challenge addressed in this thesis is navigation of autonomous vehicles through roundabouts. We advocate for the use of path following by presenting a theoretical strategy that achieves traversal of roundabout paths.

1.3 Motivation and Challenges

Most research on autonomous driving is devoted to straight line driving and steady-state cornering. Yet, roundabouts are quite commonplace [11]. Driving behavior along roundabouts differs from that of conventional driving scenarios. In Ontario, Canada, drivers are required to traverse roundabouts in a counterclockwise direction [12]. Moreover, they can only traverse the intersection if the roundabout is clear of pedestrians and other vehicles. Conventional

signalled intersections, however, allow drivers to either proceed straight, turn right, or turn left. Additionally, traffic can flow in two directions simultaneously.

Depending on the number of road junctions at a roundabout, steering requirements change. A study conducted by Zhao et al. [13] reveals that one steers a vehicle in both directions when going through a roundabout. Upon entry, a driver steers a vehicle right and then steers to the left while traversing the roundabout. Finally, the driver may steer to the right again when exiting a roundabout. But this depends on the exit the driver chooses. Considering that drivers can only enter a roundabout when it is clear, it is natural to assume that drivers accelerate their vehicles from a standstill. The steering requirements and the acceleration action indicate that roundabout traversal cannot be considered using steady-state cornering principles [14]. If vehicle dynamic simulations are required for roundabouts, it is necessary to incorporate appropriate tire models and suspension models into a vehicle dynamic simulation. This way, the behavior of general turning maneuvers can be studied. If one designs a controller for roundabout navigation using a vehicle dynamics model without these characteristics, then one cannot be assured that actual autonomous vehicles can safely navigate a roundabout.

1.4 Thesis Organization

This thesis contains vehicle modelling work and control design to facilitate roundabout navigation. Modelling efforts were made to improve a 14 degree of freedom vehicle dynamic model of a 2015 Plug-in Hybrid Electric Vehicle (PHEV) Toyota Prius [15] to characterize roundabout turn physics in detail (see Appendix A). Attention was focused on developing tire models and models of suspension kinematics to accurately simulate general turning maneuvers. Model development was facilitated by experimental procedures on an actual 2015 PHEV Toyota Prius.

The second chapter provides a comprehensive literature review on modelling and path following. The third chapter includes a study of various combined slip tire models on their accuracy in predicting combined slip tire loads. Additionally, construction of a reduced order suspension model is presented to mathematically represent suspension kinematics. The fourth chapter presents the process of constructing a reference path for navigation through

roundabouts. Next, a proposed development of a kinematic path following algorithm is presented along with an actuator controller that physically applies the commands of the kinematic path following algorithm. Finally, path following results were generated by applying the control system to the upgraded high fidelity model. The last chapter details observations and directions for further research.

Chapter 2
Literature Review

2.1 High Fidelity Modelling

The growth of computer technology has extended the capabilities of simulation software for vehicle design and analysis. Now, simulation software can be used to produce detailed dynamic models of vehicles to evaluate the performance of vehicle controllers. Commonly referred to as high fidelity models, these models can reduce the amount of experimentation required for controller testing [16, 17] . Consequently, the frequency of accidents can also be reduced because one can quickly address dangerous situations by testing controllers on high fidelity models. Because high fidelity vehicle models closely resemble real vehicles, high fidelity vehicle models can be used to perform robustness studies of controllers. There are multiple simulation platforms that allow for the construction of high - fidelity models. Each of them has their own advantages and disadvantages. Some of the popular simulation software for vehicle dynamics are:

- MSC ADAMS
- CarSim
- Simscape Multibody
- MapleSim

Throughout this work, the coordinate system in Figure 2.1 will be used to characterize the global positions and orientations of the vehicle chassis. The red dot corresponds to the front of the vehicle.

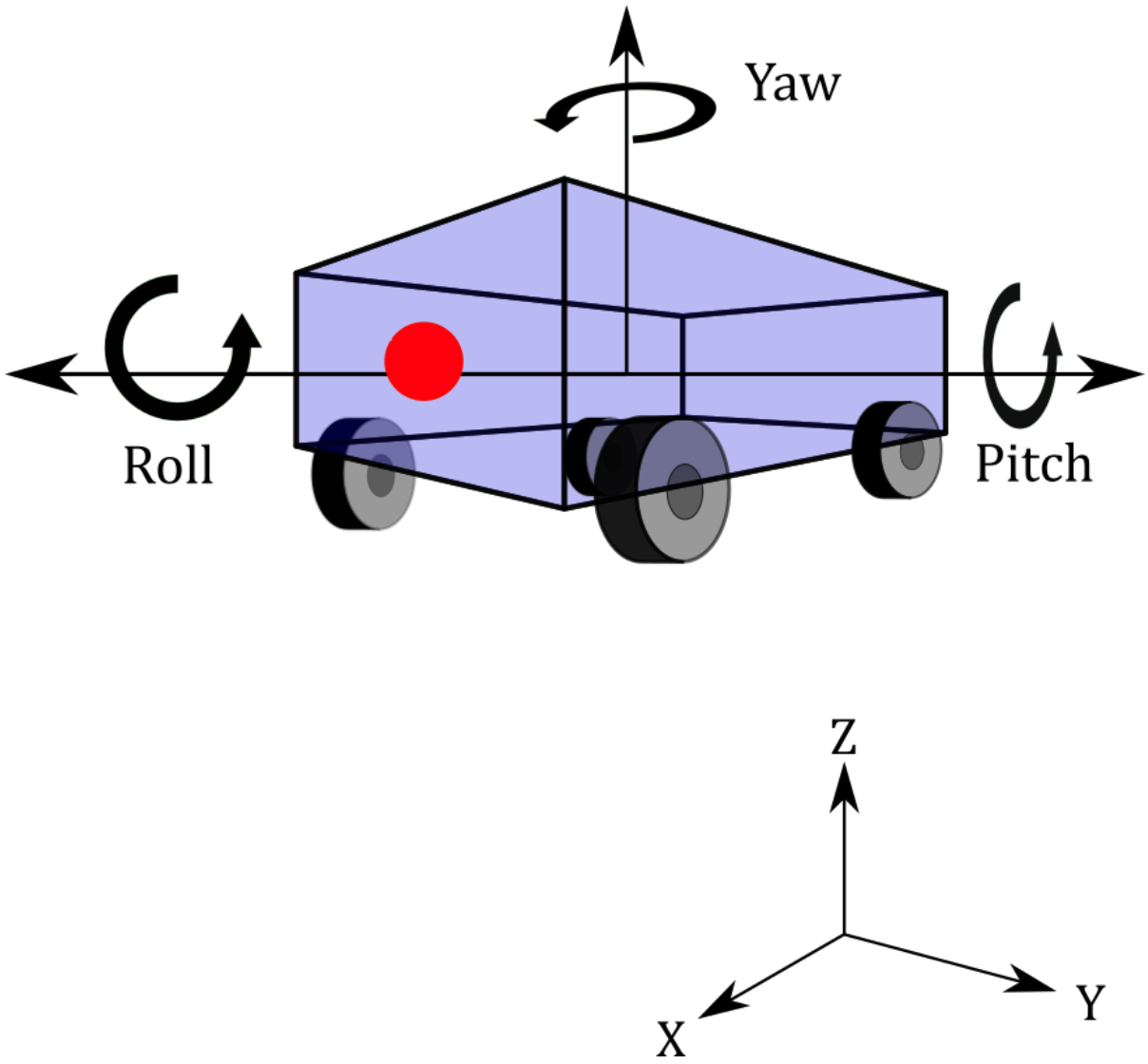

Figure 2.1 Vehicle Chassis Coordinate System

2.1.1 MSC ADAMS

MSC ADAMS is a popular multibody dynamics software with a tool called ADAMS Car specifically built for vehicle dynamic analyses [18]. ADAMS Car supports the ability to perform standard vehicle tests in a virtual environment for validation or verification purposes. For example, one can study the suspension system of a car by using ADAMS Car's four post test rig [18]. ADAMS Car employs differential algebraic equation (DAE) solvers when simulating constrained vehicle systems, where ordinary differential equations are solved

numerically while satisfying algebraic constraint relationships. This restricts its usability for real-time applications because of the computational requirements in solving DAEs.

2.1.2 CarSim

CarSim is a software package tailored specifically for virtual automobile control testing. One can design and simulate driving scenarios for contextual testing of controllers [19]. In simulating vehicles with ADAS, CarSim allows users to specify driver models and traffic environments for their testing needs. Furthermore, these simulations can be performed in real time to aid with computational efficiency studies of automobile controllers.

2.1.3 Simscape Multibody

MATLAB has a multibody dynamics tool developed for use with Simulink called SimScape [20]. SimScape provides tools to help users design controllers or to optimize system designs. Additionally, SimScape supports model deployment for hardware-in-loop (HIL) testing of controllers and C-code generation of models for model-based control design.

2.1.4 MapleSim

MapleSim is a multibody dynamics extension to Maple [21]. Unlike traditional multibody dynamics software, MapleSim relies on a graph theoretic approach to modelling [22].This extends common modelling capabilities because one can combine models from different physical domains (i.e. mechanical and electrical) to create a complete model. This feature is beneficial for modelling hybrid vehicles they contain electrical and mechanical components that interact with each other. Furthermore, MapleSim applies symbolic formulations when solving multibody dynamic equations to reduce computational time. Additionally, MapleSim has a custom component tool that allows one to create and apply novel components to high fidelity models. Nonstandard vehicle modelling elements can be made this way.

2.2 Tire Modelling

Tire forces, moments and kinematic variables are defined according to a standard coordinate system called the SAE Tire Axis System (see Figure 2.2) [29]. In this thesis, the longitudinal

forces will refer to forces in the positive SAE X-direction, the lateral forces occur in the positive SAE Y-direction and the vertical loads act in the positive SAE Z-direction.

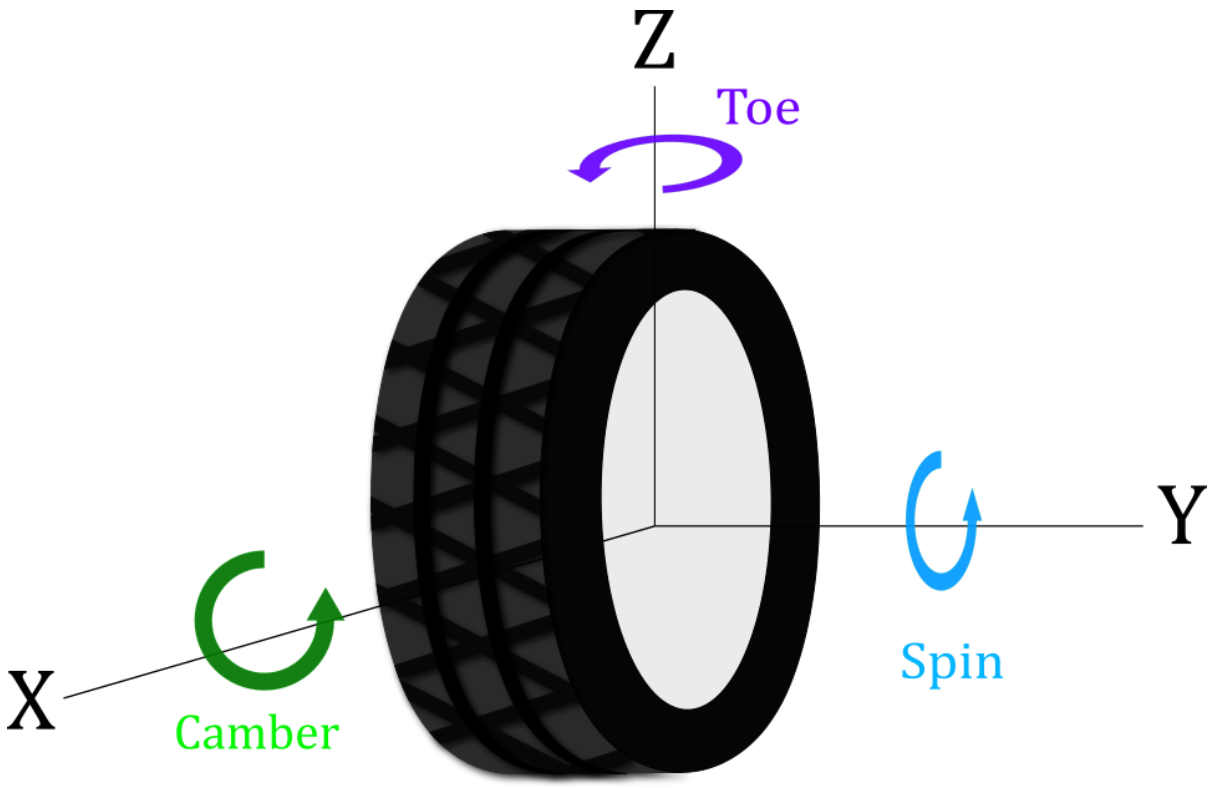

Figure 2.2 SAE Tire Coordinate System

Two important quantities associated with tire kinematics and dynamics are slip and sideslip [23, 29]. Tire slip occurs due to deformation of the tire rubber and it affects the translational motion of a tire in the SAE X-direction. Numerically, the slip ratio quantifies tire slip in the SAE X-direction by providing a measure of pure translational motion of a tire's center of mass [29]. Larger slip ratio values indicate less rolling and greater sliding action of a tire on a road surface. Physically, screeching tires during hard braking maneuvers represent large slip ratios. Sideslip is an angular measurement quantifying the deviation between a tire's heading angle (SAE X-direction) and its travel direction (see Figure 2.3). The sideslip angle (α) becomes nonzero when turning and leads to the generation of lateral forces.

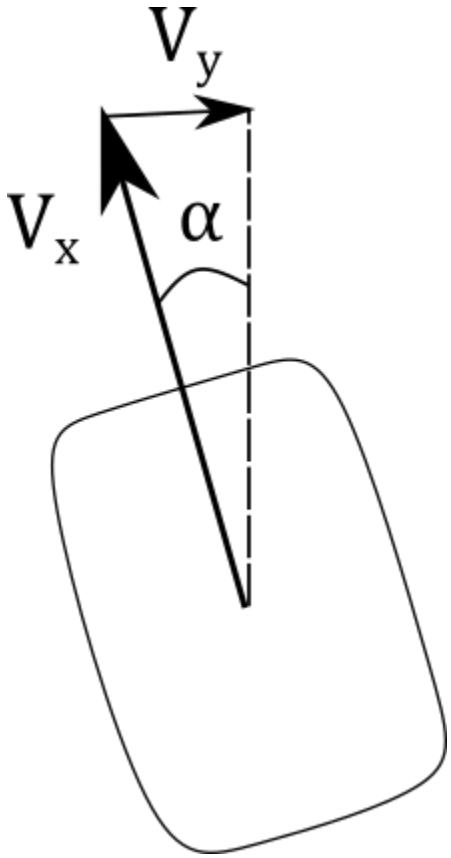

Figure 2.3 Tire Sideslip Angle

In general, tires are challenging vehicle elements to model accurately, yet the forces they experience have a profound influence on vehicle dynamics [23]. The difficulty in modelling tire forces and moments stems from characterizing the dynamic and material properties of the rubber. Tire performance can be influenced by temperature changes, inflation pressure changes and vehicle weight transfer and they occur simultaneously. Typically, tire data is generated by subjecting them to various tests on dedicated test rigs. Although reliable tire data is collected this way, the tire data is not reflected in the context of driving because the aforementioned effects cannot be reproduced simultaneously on these test rigs. It was revealed by Nordeen, that changes to the contact forces between the road and the tire have a significant impact on the lateral forces that can be generated by a tire [24] making it important when considering turning maneuvers. Turning induces shifts in vehicle weight which in turn vary the vertical

loads acting on all four tires. In turn, this affects the cornering properties of the tires. Additionally, tires warm up as vehicles are driven. This also induce changes to tire pressure. Together, these effects contribute to changes in tire performance when turning. Lastly, turning also induces nonzero moments on the tires which change tire orientation [14]. This contributes to changes in lateral forces affecting tire cornering properties.

Due to the complexity of tire behavior, there is a spectrum of proposed tire models which are appropriate for specific applications. On one end of the spectrum, there are simple linear tire models that capture the major characteristics of tire behavior [23]. These tire models are typically used for vehicle control applications because their simplicity ensures they are not computationally demanding. On the other end of the spectrum, there are complicated finite element tire models that capture rubber deformation mechanics, temperature effects and pressure effects in great detail [23]. Finite element tire models are computationally demanding, but realistic enough to be suited for tire analysis and tire development. There are, however, models which offer a compromise between detail and computational intensity. Among them, the most popular models are the Magic Formula, the Dugoff model and the LuGre model [25, 26, 27, 28].

2.2.1 Combined Slip Tire Modelling

On roundabouts, vehicles will accelerate and steer simultaneously [13]. This means tires will incur nonzero longitudinal slips and nonzero sideslip angles during a turn. According to Pacejka, Wong and Brach and Brach, this state is known as combined tire slip [23, 14, 29]. When a tire is experiencing combined tire slip, the longitudinal and lateral forces acting on a tire will be coupled causing significant changes to a tire's cornering properties. Conventional tire models, like the Magic Formula, do not capture the relationship between longitudinal and lateral loads. To accurately simulate this coupling, it is important to consider a combined slip tire force model. In the literature, most combined tire slip models were found to be data driven or developed from first principles. The data driven tire models are produced from empirically from tire load data whereas, the first principal models are developed from physical representations of tires. These tire models, however, require some data driven elements such

as parameters to make them consistent with a specific tire. Brach and Brach [29] presented a list of requirements to qualitatively evaluate combined tire slip models. They proposed that a combined tire slip model should be able to continuously map to pure slip conditions. Furthermore, when a tire locks (i.e. slip ratio is 1 or -1), the resultant of the combined slip load must be equal to μF_z where μ is the friction coefficient between the tire and the road and F_z is the vertical load acting on a tire. This requirement should hold true at any sideslip angle. It was observed that the common approach to combined tire slip modelling is to extend pure slip models to predict combined slip loads.

Bayle, Forissier and Lafon [30] developed an empirical extension of the Magic Formula for combined slip conditions using weighting functions. The weighting functions, when applied to the Magic Formula, attenuate pure slip longitudinal and lateral loads to predict combined slip loads. At pure slip conditions, the weighting functions become unity which implies this method continuously maps to pure slip conditions. The 2002 version of the Magic Formula has this model built into it [23, 31]. In 2015, Taheri and Wei [32] predicted combined slip tire loads with weighting functions that differ from those of Bayle, Forisser and Lafon. While Bayle, Forissier and Lafon developed their model for the Magic Formula, the combined slip model by Taheri and Wei was applied to a pure slip tire force model they developed. Rather than curve fitting a sinusoidal weighting function, Taheri and Wei suggested curve fitting exponential functions. Additionally, Taheri and Wei introduced a term called the residual force that accounts for tire camber effects and asymmetry of the tire geometry. Both models were shown to agree well with combined slip tire load data.

The COMBINATOR model proposed by Schuring, Wagner and Pottinger [33], is an empirical combined slip tire model that treats tire slip as a vector. The components of the slip vector are made up of the slip ratio and the sine of the sideslip angle. An important characteristic of the vector treatment of slip is that the slip vector forms a circle if the vector is varied by the angle between the slip components. The radius of the circle is equal to the resultant magnitude of the slip vector. To apply this model, pure slip tire load models must first be expressed in terms of the resultant slip magnitude. The combined slip tire loads could be found using relationships between the slip magnitude and the angle subtended by the slip

vector. An important assumption that was made in this model is that the slip vector is colinear with the resultant load. This assumption has been a source of contention in [34] and [35]. It was found by Xi and Guo that this conjecture does not hold at small slip magnitudes due to anisotropy of tires. Pottinger, Pelz and Falciola [36] tested the effectiveness of the COMBINATOR model on a set of truck and racing tires however they did not test the COMBINATOR model on tires for passenger vehicles. They found that the COMBINATOR model holds well for tires bigger than 275/80R22.5.

In a series of papers by Guo et al. [37, 38, 34, 39] the UniTire model was proposed for vehicle dynamic simulations with the capability of predicting tire loads under combined slip conditions. Using a simple physical model of tires, modified slip definitions were proposed which depend on tire deformation parameters. Guo and Sui [40] demonstrated that under combined slip conditions, the tire rubber deflects in the direction of the resultant slip they proposed. Based on this observation and tire loading measurements, Guo et al. developed a tire force model for a normalized force in the resultant direction. This resultant load is then scaled using the modified slip quantities to predict combined slip longitudinal and lateral tire loads. The UniTire model was shown to accurately predict combined tire slip loads while requiring less parameters than other tire models. Improvements to the UniTire model were made in [37] to better improve combined slip prediction capabilities and to include non-steady tire loading effects.

Based on the ideas by Guo et al, Guo and Xu [34] presented a method to predict combined tire slip loads using pure slip tire force models. This method became known as the State Stiffness method. The State Stiffness model was developed partly to address the issue of the collinearity assumption in the COMBINATOR model not holding true at small slip magnitudes. According to Guo and Xu, a tire's loading characteristics are dominated by deformation of the tire rubber at low slip magnitudes. This invalidates the collinearity assumption of the COMBINATOR model because tires have anisotropic material properties that dominate at low slip magnitudes. The State Stiffness method is a combined tire slip model that captures combined tire slip loading characteristics through the brush model [24] while including tire anisotropy. Based on the brush model, a tire's loading characteristics under

combined slip conditions are related to pure slip conditions because both conditions can produce the same deflection of a brush bristle [40, 34, 39]. Hence, they claim the stiffness of the bristles in both situations will be the same thereby establishing a connection between combined tire slip loads and pure slip tire loads.

The popular software ADAMS, by MSC Software, has two combined tire slip models available for the application ADAMS Car [41]. Users can either use a model developed by MSC Software or the weighting function model by Bayle, Forisser and Lafon. Like the COMBINATOR model, the ADAMS model also uses the slip circle. However, the slip circle is used to predict friction coefficients in the longitudinal and lateral directions under combined slip. These friction coefficients scale pure slip tire forces to predict the combined slip tire forces.

Gafvert and Svendenius [42, 35] also developed two semi - empirical combined tire slip model from the brush model. They have shown from first principles that the brush model can be used to identify invariant slip ratios and sideslip angles between pure slip tire loads and combined tire slip loads, which could be exploited to predict combined tire slip loads. Gafvert and Svendenius demonstrated in their derivations that tire loads can be separated into an adhesion part and a sliding part. The combined slip tire loads could be found by scaling these parts and then superimposing the results. Both models were shown to have similar accuracy in predicting combined tire slip loads. Gafvert and Svendenius have further developed their proposed models to include transient tire loading behavior and camber effects in [43, 44].

Van Gennip and McPhee proposed an approach to extend pure slip tire models in [45] for combined slip conditions. Firstly, the pure slip tire model is fit to tire load data at various slip ratios and sideslip angles for both the longitudinal and lateral directions. Spline interpolation curves are then used to modify the parameters of the pure slip tire model to create a continuous function that could be used to predict combined tire slip loads. As noted by Van Gennip and McPhee, the accuracy of the model depends on the number of pure slip tire load curves fit to tire load data. With more curves, better splines can be used and therefore more accurate estimates of combined tire slip loads can be found. This approach can be difficult to use if a

combined tire slip model has too many parameters because these parameters would need to be identified for more than one tire curve. Furthermore, this method is stringent on the quality of data because the accuracy depends on the goodness of fit of the pure slip tire models at various slip ratios and sideslip angles.

Nicholas and Comstock [46] introduced and extension of pure slip tire models using empirically derived mappings of the pure slip longitudinal and lateral loads. However, Brach and Brach [29] found this model does not continuously map to pure slip conditions so they made changes to the Nicholas Comstock model which became the Modified Nicholas Comstock model. The Modified Nicholas Comstock model was shown to map to pure slip conditions continuously and they require parameters that could be found from pure slip tire load data.

2.3 Suspension Kinematics and Compliance (K&C)

According to Cao et al., there are three factors that influence the behavior of suspension systems: springs, dampers and suspension kinematics and compliance (K&C) [47]. Suspension kinematics refer to displacements and changes in wheel orientation due to suspension geometry. Compliance refers to changes in a wheel's kinematics due to deformation of the suspension links and its bushings. For most vehicle modelling applications, suspension K&C are neglected. Unlike springs and damper behaviors, which could be modelled using two degree of freedom suspension systems (i.e. quarter car suspension models), modelling suspension K&C require complicated multibody dynamic representations. This is chiefly due to the need for considering the complicated geometry of a vehicle suspension system.

According to Stoll and Reimpell, the geometry of a vehicle suspension system profoundly influences vehicle performance [48]. For instance, negative camber angles reduce steering effort while cornering however too much camber causes tire wear to accelerate. Additionally, suspension kinematics affect vehicle roll behavior when cornering. Shim and Veluswamy conducted a study of suspension kinematics on vehicle roll stability [49]. They found that toe and camber angles can significantly affect the roll response of a car when turning. Moreover, suspension kinematics can also influence the characteristics of vehicle tires. Camber angles

contribute to lateral forces and overturning moments when cornering by generating a force called camber thrust [14].

In addition to suspension kinematics, deformation of suspension links and bushings also contribute to a vehicle's handling performance. This deformation is known as suspension compliance. Park and Nikravesh demonstrated that deflections of suspension bushings is important when studying vehicle Noise, Vibration and Harshness (NVH) [50]. Likewise, Blundell found suspension compliance significantly affects toe kinematics [51].

Most vehicle suspension systems take on one of three different architectures [52]. The MacPherson strut is an assembly consisting of a lower control arm connecting the wheels to the chassis and a strut connected to the shock absorber. It is the least expensive architecture, so it is commonly found on passenger vehicles. The double wishbone suspension consists of two control arms where one of the control arms attaches to the shock absorber of a vehicle. At the cost of increased tire wear, double wishbone suspension systems are commonly found on luxury vehicles and sports cars because they can reduce negative camber angles on wheels during turning maneuvers to enhance vehicle cornering performance. Lastly, the multi-link suspension architecture features a collective of flexible links connecting the chassis to the wheels and the shock absorbers to the wheels. This structure is commonly found on high end race cars and all-terrain vehicles. Multi-link suspension systems offer tremendous performance tuning flexibility because each of the links can be independently adjusted to generate various wheel alignment behaviors.

Reproducing the architectures for multibody dynamic simulations can be a demanding process. Suspension parameters would be required from experimentation, and multiple constraints need to be both imposed and enforced. Due to the complexity of suspension K&C models, they would not be suitable for application with vehicle control design. High fidelity vehicle models are often incorporated with hardware-in-loop (HIL) testing of controllers and are required to simulate in real time [53]. However, a complicated suspension K&C model would slow computation time. This motivates a requirement for simpler suspension K&C models that maintain a high degree of accuracy.

Suspension kinematics and compliance data is typically generated using a testing procedure referred to as a K&C test [54]. A vehicle is hoisted on a test rig where each wheel is supported by a moveable pad. The pads are moved in various ways to excite changes in tire position and orientation. Along with changes in a vehicle chassis, the motion of the tires is measured.

One approach to creating reduced order suspension K&C models is to use a Single degree of freedom Equivalent Kinematic (SEK) joint [55]. The SEK joint captures the relative motion between a vehicle wheel and a vehicle chassis by replacing the suspension geometry with a holonomic constraint. The constraint, however, is a reference path specified parametrically and is therefore not a traditional holonomic constraint [56]. Simulations of a SEK joint used to model suspension K&C showed a significant reduction in computation time compared to typical multibody dynamic suspension models [55]. This is partly due to the symbolic formulations associated with SEK joints.

2.4 Path Following

The goal of a path following problem is to ensure that a system smoothly merges onto a predefined reference path and then traverse that path without deviating from it [57, 58]. Path following can therefore, be considered a variation of a trajectory tracking problem because a system is tasked to approach and follow a defined trajectory rather than match a time varying reference signal. Path following problems offer some advantages over standard trajectory tracking problems. They can reduce control effort, offer stronger robustness properties, reduce likelihood of controller saturation and mitigate transient effects too [57].

From a theoretical perspective, one of the principal advocates of path following is in the control of nonminimum phase systems [59, 60]. According to Aguiar et al., nonminimum phase systems have performance limitations when regulating them using standard trajectory tracking methods. However, they showed that by recasting the regulation problem as a path following problem, nonminimum phase systems can be rendered stable by imposing an appropriate timing law between a reference path location and time rather than a control law. In the case of nonminimum phase linear systems, Dagic and Kokotovic provided sufficient conditions to stabilize these systems and provided a procedure for designing stabilizing controllers for these

systems [61]. Dagic and Kokotovic proved that nonminimum phase linear systems can be stabilized if the origin of their state spaces lies in a convex region of admissible timing laws. Additionally, the reference path is required to be bounded for all parameter values. Expanding on the work by Aguiar et al. and the work by Dagic and Kokotovic, Miller and Middleton studied the efficacy of using path following strategies to improve the performance of nonminimum phase linear systems [62]. Using the mathematical properties of a nonminimum phase system, they derived conditions to reduce performance costs through path following perspectives. Moreover, they developed computational tools to determine cost functions that would allow one to synthesize controllers that would improve performance. Effectively, they presented ideas to distinguish trajectories that lead to desired performance and a computational framework for path following control design along those trajectories.

In addition to alleviating performance limitations in nonminimum phase systems, path following strategies have been utilized for navigating robots [63, 64], unmanned aerial vehicles (UAVs) [65], marine vehicles [66, 67, 68] and autonomous cars [69, 70]. Among the strategies presented for vehicle navigation, are different stability and performance characteristics.

In a survey of various path following strategies for unmanned aerial vehicles, path following controllers can be typically classified as either geometric or control theoretic [58]. Geometric methods rely on physical relationships between reference paths and vehicles to devise routes for a vehicle to take. Whereas control theoretic methods use external control laws to direct vehicles toward reference paths.

Commonly, geometric approaches rely on a principle known as “virtual targets” which define destinations and directions of travel for vehicles [71]. Three popular techniques that use the virtual target concept are the pure pursuit, line-of-sight method (LOS) and the nonlinear guidance law (NLGL) [67, 72, 73]. The pure pursuit algorithm defines a target point on a reference path and a vehicle is tasked to directly approach that point. The LOS method, however, uses a vector attached to a vehicle that defines a heading direction for it. As the vehicle moves, the vector updates until the vehicle reaches the virtual target point on the reference path. In the nonlinear guidance law, a circle of some radius is defined around the

vehicle and a virtual target point is specified where the circle intersects the reference path. Motion commands are then specified to have the vehicle smoothly approach the virtual target. Rather than solely using virtual target points, modifications were presented where Frenet-Serret frames were attached to the virtual target points [70, 71]. This allowed the virtual target points to be regarded as virtual vehicles and dynamics could be assigned to the virtual vehicle for greater flexibility.

According to Rubi et al., the most popular control theoretic path following algorithms are backstepping and feedback linearization [57]. Backstepping uses a series of error functions to recursively determine control inputs that make each error function asymptotically approach zero. The authors remark that backstepping approaches create large regions of stability and offer robustness against disturbances. Feedback linearization is often paired with backstepping in path following problems and it allows a nonlinear path following problem to become linear using a control law that negates nonlinear terms.

A notable approach involving the control theoretic methods is to recast path following problems as set stabilization problems. Nielsen et al. proposed a variant of feedback linearization where a reference path is transformed into a set that can be rendered stable using a feedback control law [74, 75]. The authors state this variant offers flexibility for path following problems because one can separately stabilize the path and specify motion requirements for merging and traversal [75]. Applied to an aircraft, the authors noticed the aircraft can merge and traverse closed reference paths and maintain bounded roll motion [76]. El-Hawwary and Maggiore developed a passivity based approach that would make a reference path into an asymptotically stable set [77]. The proposed feedback law is made up of two control inputs to handle traversal and merging, respectively. One of the control inputs renders the reference path inescapable by enforcing a condition and the other control input makes the reference path stable with respect to a function. When applied to a path following problem involving a unicycle model and an elliptical path, the ellipse becomes globally stable and the controller appropriately orients the unicycle. For applications to rigid bodies, Kapitanyuk et al. proposed a passivity-based controller to stabilize reference paths transformed into sets [78]. Firstly, the authors defined error functions and velocity requirements based on a reference path.

Next, the translational and rotational dynamics of a rigid body were expressed in terms of the error functions and required velocities. The authors proposed feedback control laws for both the translational forces and rotary moments that would make the dynamics of a rigid body stable.

From the perspective of path following error, Sujit et al. revealed, in their study, that vector field algorithms can lead to the smallest errors in path following [58]. Notably, vector field approaches were found to be popular in path following problems involving aerial vehicles. Lawrence et al. presented a vector field approach using Lyapunov functions for autonomous flight navigation [79]. The Lyapunov functions are used to specify attractive locations and velocity vector fields that direct an aircraft to those locations. By switching the vector fields between attractors, aircrafts can follow paths composed of lines and arcs. They have shown mathematically that the algorithm leads to globally stable behavior. Nelson et al. also developed a vector field path following algorithm for aircrafts, but their vector field assigns an orientation based on an aircraft's position [65]. Combining a vector field approach with sliding mode control, this vector field was shown to produce small path following errors for paths composed of straight lines and arcs in the presence of wind disturbances. Like Nelson et al., Yajing et al. presented a vector field algorithm that is combined with sliding mode control [80]. Yajing et al. first formulated the error kinematics of an unmanned aerial vehicle using a Frenet-Serret frame on a parametric function. Then they define a vector field that assigns an orientation based on the error kinematics. They have shown smooth merging and traversal along reference paths defined by splines in the presence of wind. Liang and Jia presented a systematic approach to vector field construction for flight navigation that could be used on a wide variety of reference paths beyond straight lines and arcs [81]. Liang and Jia employed the use of a decomposition approach to systematically construct a composite velocity vector field that is made up of two vector fields. The conservative vector field creates a vector field tangential to the reference path and the solenoidal vector field makes a normal vector field to the reference path. When combined, the composite vector field leads to convergence of UAVs to the reference path.

Chapter 3
Vehicle Modelling

3.1 Introduction to Vehicle Modelling

In this chapter, the modelling of combined slip tire models and suspension (K&C) will be discussed. The first part is about the experimental equipment used for data collection. Next, a description of the physics of combined slip tire behavior is presented followed by a study of combined slip tire force models. The study consisted of popular combined slip tire force models and tire force data where the models were tested for their ability to predict the tire force data. Finally, an overview of suspension (K&C) is presented. The various components of suspension (K&C) are described and their impacts on vehicle performance is discussed. Development of the SEK joint follows.

3.2 Experimental Equipment

3.2.1 Vehicle Measurement System (VMS)

The VMS (Figure 3.1) is a sensory system developed by A&D Technology to collect tire loading and tire kinematic data, while driving a vehicle [82]. The size and value of the system make it inappropriate for use on public roads, so it was used for specialized driving maneuvers performed on a vehicle test track. The VMS is made up of a collective of three major sensor units.

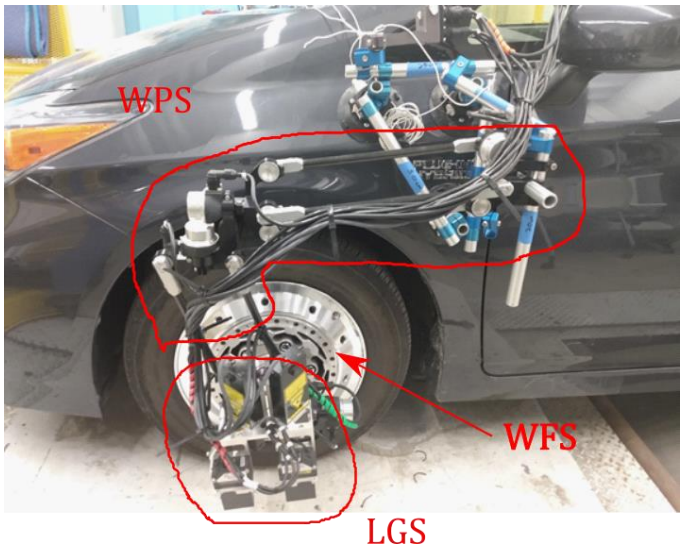

Figure 3.1 Vehicle Measurement System Attached to Toyota Prius

The Wheel Force Sensor (WFS) is a custom wheel hub containing strain gauges which measure the forces and moments acting on a tire. These measurements are according to the SAE tire axis system [83] (see Figure 2.2). The Wheel Position Sensor (WPS) is an assembly of links and encoders that measure displacements and changes in tire orientation. The displacements and changes in orientation are also measured according to the SAE tire coordinate system. The Laser Ground Sensor (LGS) uses a series of lasers to measure tire velocities and track changes in tire radii.

3.2.2 Inertial Measurement Unit (IMU)

The VBOX 3i is an Inertial Measurement Unit (IMU) by Racelogic [84] that was mounted on top of the Prius. The IMU measured translational and rotational accelerations of the Prius's chassis. Unlike conventional IMUs, the VBOX 3i included a Global Positioning System (GPS) that measured the Prius' position and heading direction. Since the IMU was not positioned at the center of mass of the Prius, coordinate transformations were made to express the measurements at the center of mass.

3.2.3 Wheel Dolly

The RL1 rotating dolly, from GKS-Perfekt, is a wheeled mobile support used to transport heavy tools and equipment [85]. The wheel dolly consists of three wheels connected to a base using swiveling connectors. A rubber pad is attached to the top of the base to act as a non-slip surface. The dolly, rated with a maximum weight capacity of 10kN, was used to support individual wheels for the SEK joint test [85].

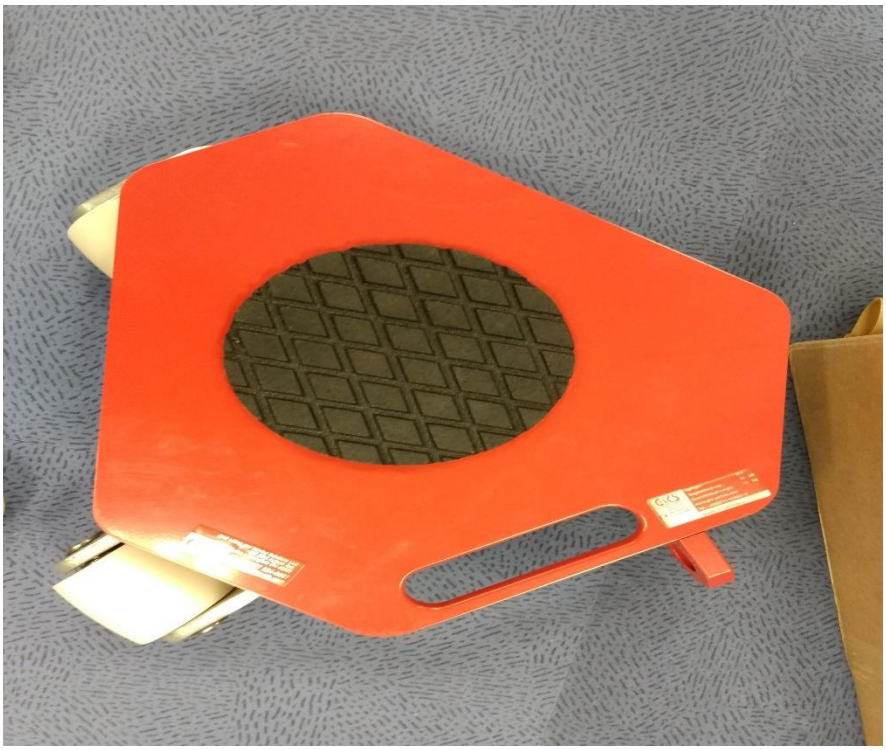

Figure 3.2 GKS Wheel Dolly

3.3 Combined Slip Tire Modelling

Modelling combined tire slip behavior requires an understanding of the friction ellipse (see Figure. 3.4), which highlights an inverse relationship between the longitudinal load and lateral load generated by a tire under combined slip [14, 86, 23]. The blue lines represent lines of constant sideslip angles with varying slip ratios and the red lines show constant slip ratios with varying sideslip angles. The friction ellipse implies that as the sideslip angle (α) of a tire increases, the amount of longitudinal force (F_x) generated by the tire reduces. Similarly, if the

slip ratio (λ) increases then the lateral load (F_y) generated by a tire abates. The limits of the friction ellipse depend on the friction coefficients of a tire in the longitudinal and lateral directions. If a tire shows weak anisotropic behavior, the friction ellipse can be approximated as a friction circle because the friction coefficients in the lateral and longitudinal directions will be similar. The friction ellipse indicates that this behavior is continuous for all combinations of the sideslip angle and the slip ratio. Additionally, when either the slip ratio or sideslip angle is zero, a tire exhibits pure slip behavior. To agree with the friction ellipse, an appropriate combined tire slip model should reflect the inverse relationship between the longitudinal load and lateral load shown by the ellipse. In addition to this agreement, the models should also be continuous functions of slip ratio and sideslip angle and that continuity should extend to pure slip conditions. Brach and Brach [86] examined the use of the friction ellipse as a model to predict combined tire slip loads and they demonstrated that the friction ellipse should not be used as a tire force model. When compared with experimental data, the friction circle tends to be considerably conservative when predicting tire forces and the limits of frictions. Thus, the friction circle serves as a guide to characterizing combined slip tire forces. This necessitates combined slip tire force models that reduce conservatism. With a less conservative model that better reflects the relationship between tire forces, the high fidelity model's tire properties would be more consistent with that of a Toyota Prius. Therefore, we could better infer how a Toyota Prius would move with a path following controller installed.

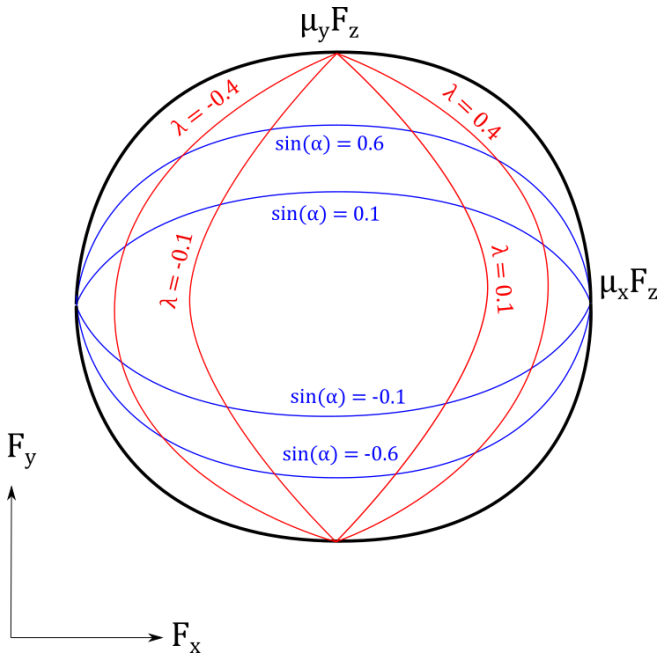

Figure 3.3 The Friction Ellipse

A physical understanding of combined tire slip behavior can be developed by studying a physical tire model called the brush model [23, 87]. Originally, the brush model was created as a tool for understanding tire loading behavior, but authors found that the brush model could be used to develop combined tire slip models. The brush model treats the rubber carcass of the tire as a series of thin brush bristles. Pacejka, Gafvert and Svendenius [23, 87, 35] showed that this view of a tire reveals that tire load curves can be broken down into two regions (see Figure 3.5). At low slip ratios and sideslip angles, tire loads are primarily generated by deformation of the bristles. This area is called the adhesion region because the brush bristles stick to the road surface [35, 42, 87]. The tire loads in the adhesion region vary linearly with the slip ratio and sideslip angle because tire rubber has elastic material behavior. As a slip quantity grows some of the bristles in the tire contact patch begin to transition into a sliding mode. This causes a tire loading curve to become nonlinear. Although the entire contact patch is no longer in the adhesion region, this part of the curve is still considered to be within the adhesion region [35, 42, 87]. Beyond a certain limit, all the brush bristles no longer deform so they begin to slide against the road surface. This creates the sliding region in a tire load curve where the tire loading characteristics are nonlinear. In the sliding region, tire loads are dominated by dry

friction forces and this causes tire load curves to saturate at large slip ratios or large sideslip angles. Within the context of the friction ellipse, Brach and Brach [86] have indicated that tire forces within the friction ellipse are forces caused by deformation of the tire carcass and that full steering control is maintained. Beyond the friction ellipse, tire forces are caused by sliding of the carcass and the relationship represented by the friction ellipse no longer holds.

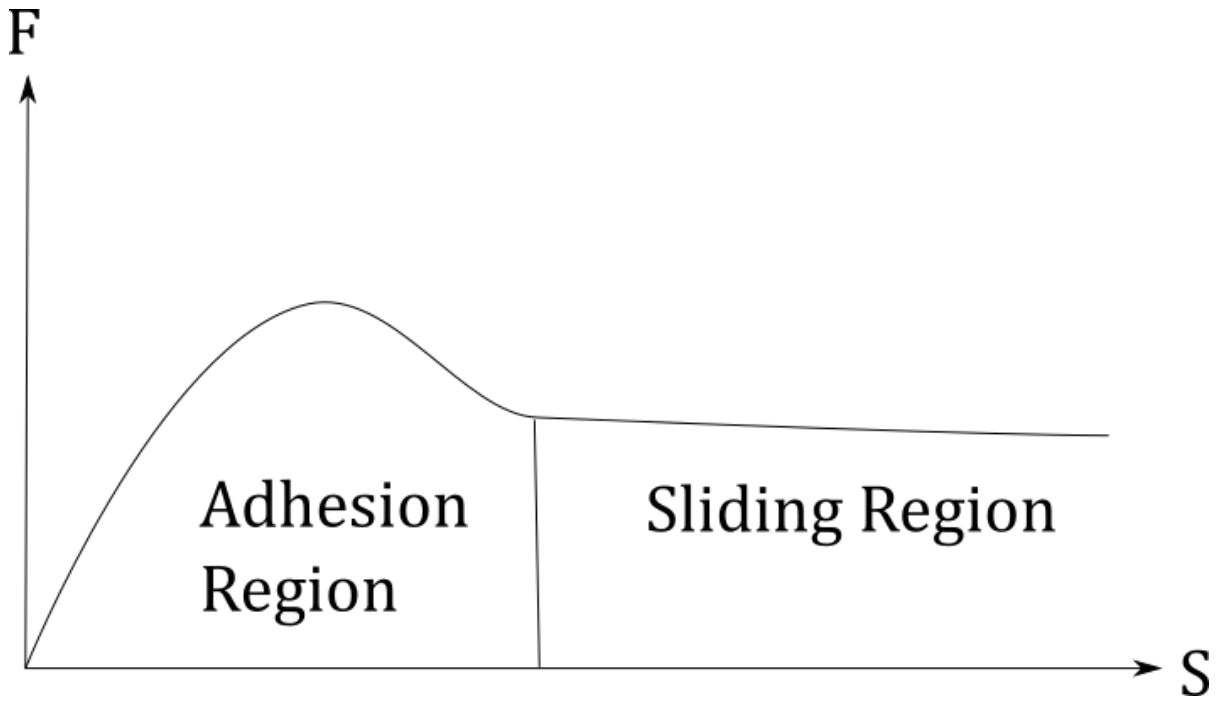

Figure 3.4 Tire Load Curve

Four combined tire slip models were compared for their accuracy in predicting combined tire slip loads with respect to tire load data from track testing. The chosen models were the:

- COMBINATOR Model
- State Stiffness Model
- ADAMS Model
- Region Invariant Slip Model

These combined tire slip models were chosen because they required little to no additional parameters beyond the pure slip tire models and their generality allows them to be paired with many static friction pure slip tire force models. Additionally, model fitting is not required for these models because they determine combined slip tire loads using predefined relationships involving pure slip tire models.

3.3.1 COMBINATOR Model

Applying the COMBINATOR model requires determining two quantities stemming from the slip circle: the resultant slip, *s*, and the joint heading angle, β, which can be computed using (3.1) and (3.2) [33]. The COMBINATOR model relies on a notion that tire slip quantities are confined to a circle called the slip circle. Equation (3.1) provides a radial measure of the slip circle for a given combination of the slip ratio and sideslip angle. Likewise, (3.2) provides an angular measurement for a slip state.

$$S = \sqrt{\lambda^2 + \sin^2(\alpha)}, \tag{3.1}$$

$$\beta = \arctan\left(\frac{\sin(\alpha)}{\lambda}\right) \tag{3.2}$$

The resultant slip from (3.1) replaces the slip quantities in a pure slip tire force model and a resultant tire load is found as in (3.3)

$$F(s, \beta) = F_{x0}(s)\cos^2(\beta) + F_{y0}(s)\sin^2(\beta) \tag{3.3}$$

where F represents the resultant tire load based on the slip circle. Finally, combined slip tire loads can be found by scaling the resultant tire load in (3.3) using the joint heading angle in (3.2).

$$G_x = F(s,\beta)\cos(\beta),$$
$$G_y = F(s,\beta)\sin(\beta) \tag{3.4}$$

where G_x and G_y are the combined slip longitudinal and lateral loads, respectively.

3.3.2 State Stiffness Model

The state stiffness model introduces a quantity called the state stiffness which is defined in (3.5).

$$K_i = \frac{F_i}{S_i} \tag{3.5}$$

where i is either the longitudinal direction or lateral direction (x or y, respectively) and S_i is the corresponding slip quantity. Visually, the state stiffness represents the slope of a secant line that connects a pure slip tire load with a slip quantity on a tire load curve (see Fig. 3.6).

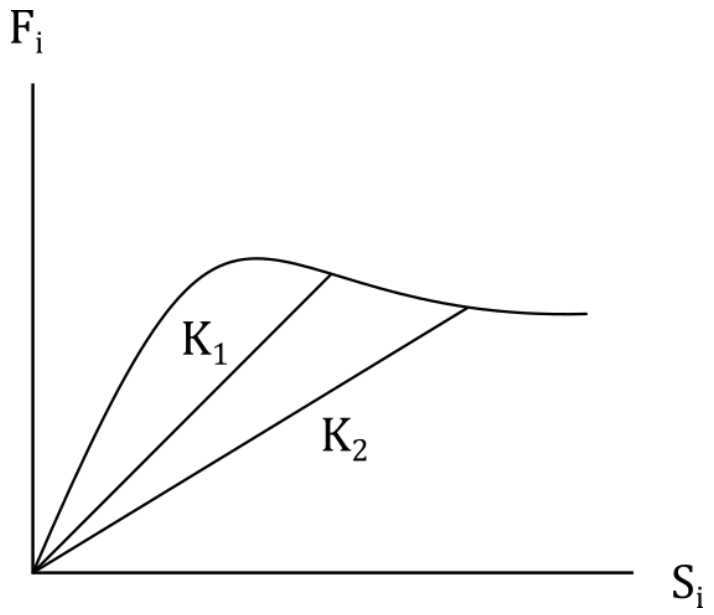

Figure 3.5 State Stiffness Representation

As proposed by Xu and Guo [34], for a given deflection of the tire carcass under combined slip conditions an equivalent deflection of the tire carcass under pure slip conditions could be

found. In either case, the state stiffness is the same. Therefore, the state stiffness could be found using the resultant slip rather than individual slip quantities. Moreover, the resultant slip can be passed as an argument to the pure slip tire force models.

$$K_i \approx \frac{F_{i0}(S)}{S} \tag{3.6}$$

Finally, the state stiffness in (3.6) scales the individual slip quantities to output the combined slip tire loads

$$G_i = K_i S_i \tag{3.7}$$

3.3.3 MSC ADAMS Model

The combined slip tire model produced for MSC ADAMS is a variation of the COMBINATOR model that was developed internally [41]. The ADAMS model uses relationships to vary friction coefficients (μ_x, and μ_y) that scale pure slip tire loads as expressed in (3.7) – (3.10).

$$\mu_{x,act} = \frac{F_{x0}}{F_z}, \qquad \mu_{y,act} = \frac{F_{y0}}{F_z} \tag{3.7}$$

$$\mu_{x,max} = \frac{F_{x,max}}{F_z}, \qquad \mu_{y,max} = \frac{F_{y,max}}{F_z} \tag{3.8}$$

$$\mu_x = \frac{1}{\sqrt{\left(\frac{1}{\mu_{x,act}}\right)^2 + \left(\frac{\tan\beta}{\mu_{y,max}}\right)^2}}, \quad \mu_y = \frac{\tan(\beta)}{\sqrt{\left(\frac{1}{\mu_{y,act}}\right)^2 + \left(\frac{\tan\beta}{\mu_{x,max}}\right)^2}} \tag{3.9}$$

$$G_x = \frac{\mu_x}{\mu_{x,act}} F_{x0}, \qquad G_y = \frac{\mu_y}{\mu_{y,act}} F_{y0} \tag{3.10}$$

where β is defined as in (3.2).

3.3.4 Region Invariant Slip Model

Similar to the claim made by Xu and Guo, Gafvert and Svendenius [87, 35] showed using the brush model that for a given combined slip condition, an equivalent pure slip condition can be found and that a relationship can be established between the two. However, they derived this condition by studying the behavior of a tire contact patch as opposed to a single bristle. Considering that a contact patch gradually transitions from full adhesion to full sliding, the contact patch has an adhesion area and a sliding area that changes based on the slip ratio and sideslip angle. Gafvert and Svendenius argued that similar sized adhesion and sliding areas of the contact patch can be found from pure slip results. They call the slip ratios and sideslip angles that generate these areas, region invariant slips. Computing the region invariant slip tire forces requires new slip quantities, defined by (3.11), related to the old ones.

$$\sigma_x = \frac{\lambda}{1-\lambda}, \quad \sigma_y = \frac{\tan(\alpha)}{1-\lambda} \tag{3.11}$$

Next, a normalized slip and normalized sideslip angle are found using the slip quantities in (3.12).

$$\psi(\sigma_x, \sigma_y) = \sqrt{\left(\frac{\sigma_x}{\sigma_x^\circ}\right)^2 + \left(\frac{\sigma_y}{\sigma_y^\circ}\right)^2}, \qquad \phi = \arctan\left(\frac{\psi(0, \sigma_y)}{\psi(\sigma_x, 0)}\right) \tag{3.12}$$

The normalized slip relies on two parameters σ_x°, σ_y° called limit slips. These are the slip values from pure slip tire models where a tire's loading behavior changes from full adhesion to full sliding. This parameter can be identified using a pure slip tire load curve as shown figure 3.5 just slightly beyond the peak force. When $\psi < 1$, the contact patch is in the adhesion region and when $\psi \geq 1$, the contact patch is in the sliding region. Using the limit slips, the region invariant slips can be found using (3.13).

$$\sigma_x^{reg} = \sigma_x^\circ \sqrt{\left(\frac{\lambda}{1-\lambda}\frac{1}{\sigma_x^\circ}\right)^2 + \left(\frac{\tan(\alpha)}{1-\lambda}\frac{1}{\sigma_y^\circ}\right)^2}\, sgn(\lambda), \tag{3.13}$$

$$\sigma_y^{reg} = \sigma_y^{\circ}\sqrt{\left(\frac{\lambda}{1-\lambda}\frac{1}{\sigma_x^{\circ}}\right)^2 + \left(\frac{\tan(\alpha)}{1-\lambda}\frac{1}{\sigma_y^{\circ}}\right)^2}\, sgn(\alpha)$$

The normalized slip in (3.12) is then inputted into (3.14) to determine the proportion of the contact patch that is sliding region.

$$\theta(\psi) = \frac{\psi(3-2\psi)}{3\rho(1-\psi)^2 + \psi(3-2\psi)} \tag{3.14}$$

where ρ is a parameter that is defined as the ratio of the tire static friction and kinetic friction coefficients. Unless the tire has strong anisotropic properties, these friction coefficients are usually assumed to be the same in both the longitudinal and lateral directions. Finally, the region invariant slips in (3.13) are passed as arguments into pure slip tire force models and scaled using the proportion in (3.14) to individually compute the adhesion and sliding loads.

$$\begin{aligned} F_{ax} &= \big(1-\theta(\psi)\big)F_{0x}\big(\sigma_x^{reg}\big)\cos(\phi), \\ F_{ay} &= \big(1-\theta(\psi)\big)F_{0y}\big(\sigma_y^{reg}\big)\sin(\phi), \\ F_{sx} &= \theta(\psi)F_{0x}\big(\sigma_x^{reg}\big)\cos(\phi), \\ F_{sy} &= \theta(\psi)F_{0y}\big(\sigma_y^{reg}\big)\sin(\phi) \end{aligned} \tag{3.15}$$

The F_a terms are the adhesive loads and the F_s terms are the sliding loads. The combined slip loads can be found by superimposing the adhesive and sliding loads in (3.16).

$$G_x = F_{ax} + F_{sx}, \;\; G_y = F_{ay} + F_{sy} \tag{3.16}$$

3.4 Comparing Combined Slip Tire Models

The combined slip tire models listed did not have associated error measurements. This can be a source of confusion for one when selecting a model to use for vehicle dynamic studies. Although they were shown to be accurate, an error analysis would allow one to differentiate these tire models from an application standpoint. To clarify the accuracy of these tire models, we present an error analysis of them with respect to driving data.

Combined tire slip conditions were created by following the approach proposed by Van Gennip and McPhee [45]. The Toyota Prius was accelerated to a specific speed and then braked aggressively while steering the vehicle to the left or right until the vehicle came to a stop. This maneuver was performed at speeds of 50km/h, 60km/h and 70km/h allowing load data at various slip ratios and sideslip angles to be generated. This test generated data only for combined braking and cornering, so symmetry was assumed for the acceleration case. Equations (3.18) and (3.19) show the definitions of slip and sideslip, respectively, that were used with the data from the VMS. This definition for the slip ratio was used instead of the slip ratio definition in SAE J670 [83] because the slip ratio in SAE J670 becomes singular when the longitudinal speed of a vehicle is small as would be the case when the Prius came to a halt.

$$\lambda = \frac{(R_e\omega - V_x)}{\max\,(V_x)} \tag{3.17}$$

$$\alpha = \arctan\left(\frac{V_y}{V_x}\right) \tag{3.18}$$

Longitudinal and lateral load data sets from each trial of the test were isolated and compiled together. Next, these loads were normalized with respect to the vertical load to eliminate the dependence of the longitudinal and lateral load on the vertical load. Finally, the normalized

longitudinal load and normalized lateral load were plotted with respect to the slip ratio and sideslip angle respectively as shown in Figures 3.7 and 3.8 for a tire corner.

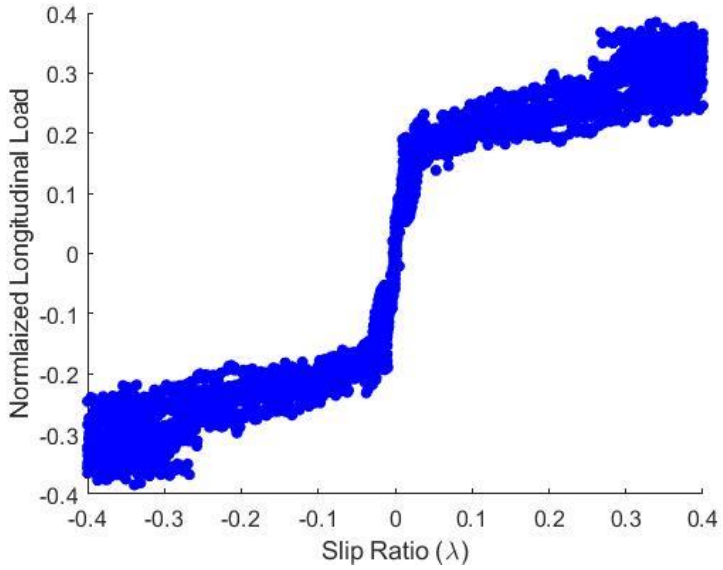

Figure 3.6 Normalized Longitudinal Tire Load

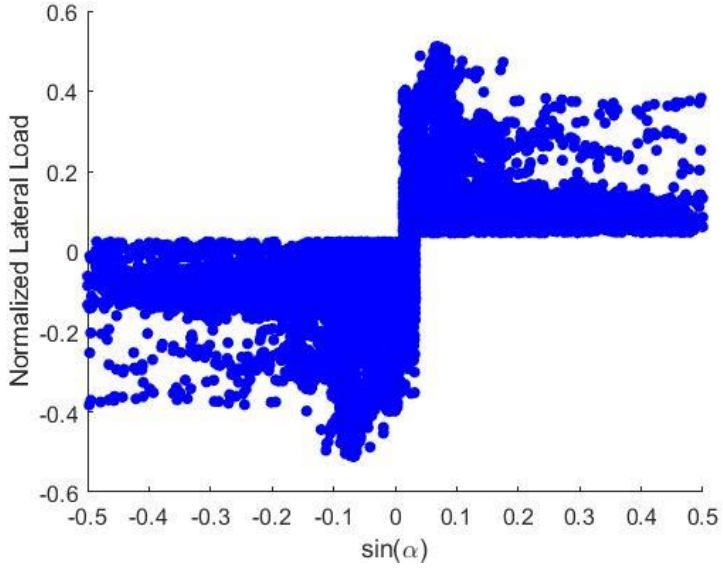

Figure 3.7 Normalized Lateral Load

Considering that tire data is typically obtained from tires mounted on dedicated test rigs [23], this data is unique because it was collected while driving on a test track. Nordeen pointed out that during general turning maneuvers, tire forces can change considerably [24]. For instance, load transfer due to chassis motions cause fluctuations in the vertical loads exhibited by tires. This results in changes to the lateral loads. Unlike test rigs where vertical loads can be kept constant, standard data processing techniques are not applicable to tire load data from driving [88, 89]. However, comparing combined slip tire force models to the driving data sets could act as a test of robustness. If these combined slip tire models are reliable, then they should be able to predict combined slip tire loads under driving scenarios with some degree of accuracy.

In this study, the 1987 Magic Formula, proposed by Pacejka, Nyborg and Bakker [27] was extended to predict combined slip tire friction forces using the previously mentioned models. The Magic Formula is a static friction empirical tire model that predicts pure slip tire loads through a pair of functions involving quantities from a tire's motion. These functions require the tire slip ratio, sideslip angle and the vertical load acting on a tire. Equations (3.19) and (3.20) show the Magic Formula relationships where one of the functions predicts pure slip longitudinal tire loads (F_{x0}) and the other predicts pure slip lateral tire loads (F_{y0}). To apply the Magic Formula to a tire, one must fit parameters in the equations to tire load data. Although the Magic Formula has gone through multiple revisions, the 1987 Magic Formula was chosen here for its simplicity. While the 1987 Magic Formula requires 4 parameters (B, C, D, E) for the longitudinal and lateral directions respectively, successive versions require a significantly greater number of parameters [23, 31].

$$F_{x0} = D_x \sin\left[\mathrm{C_x} \arctan\left(B_x\lambda - E_x\left(\arctan\left(B_x\lambda\right)\right)\right)\right] F_z \tag{3.19}$$

$$F_{y0} = D_y \sin\left[\mathrm{C_y} \arctan\left(B_y\alpha - E_y\left(\arctan\left(B_y\alpha\right)\right)\right)\right] F_z \tag{3.20}$$

The normalized longitudinal load was separated by sideslip angles and the normalized lateral load was separated by slip ratio. Each of the aforementioned combined slip tire models were evaluated at those slip states. As an error metric, the mean squared error (MSE) between the normalized loads predicted by the models and the loads collected from the VMS were computed to determine the accuracy of the models. The expression for MSE is expressed in (3.21).

$$MSE = \frac{\left(G_i(\hat{\lambda}, \hat{\alpha}) - \hat{G}_i(\hat{\lambda}, \hat{\alpha})\right)^2}{Number\ of\ Data\ Points} \tag{3.21}$$

The longitudinal and lateral directions are referenced by the index, i. The computation of the MSE requires substituting slip ratios and sideslip angles ($\hat{\lambda}$ and $\hat{\alpha}$ respectively) from the VMS to the combined slip tire models. We compare the determined normalized load (G_i) with a corresponding load data point from the same slip state ($\hat{G}_i$). The MSE computation was performed over the full range of available slip ratios and sideslip angles.

This error metric was chosen over root mean squared error (RMSE) because RMSE tends to penalize small errors greatly. Naturally, one can expect some degree of error because the driving conditions under which the data was generated differ from standard testing scenarios. Thus, MSE ensures these effects do not heavily influence the comparison. The MSE of each tire model is presented in Table 3.1 separated by the normalized longitudinal and normalized lateral loads, respectively.

Table 3.1 Mean Squared Error Results

Model	Normalized Longitudinal Load MSE	Normalized Lateral Load MSE
COMBINATOR Model	0.0634	0.0997
State Stiffness Model	0.0517	0.0522
MSC ADAMS Model	0.0650	0.1053
Region Invariant Slip Model	0.0533	0.0554

To understand the nature of errors in model accuracy, it is necessary to visualize the tire models by plotting them. We plot the longitudinal tire forces predicted by each combined slip tire models based on various sideslip angles. Similarly, we plot the lateral tire forces for various slip ratios.

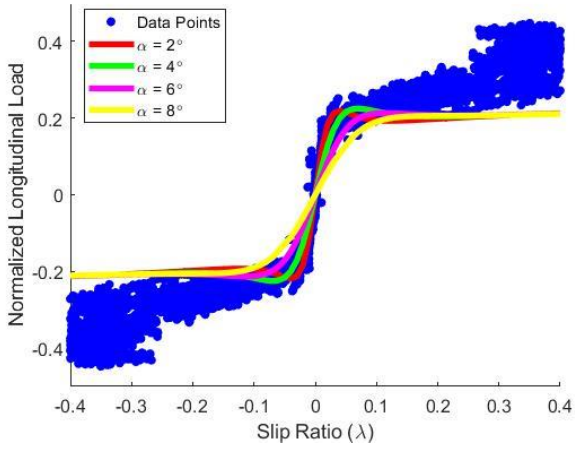

Figure 3.8 COMBINATOR Model in Longitudinal Direction

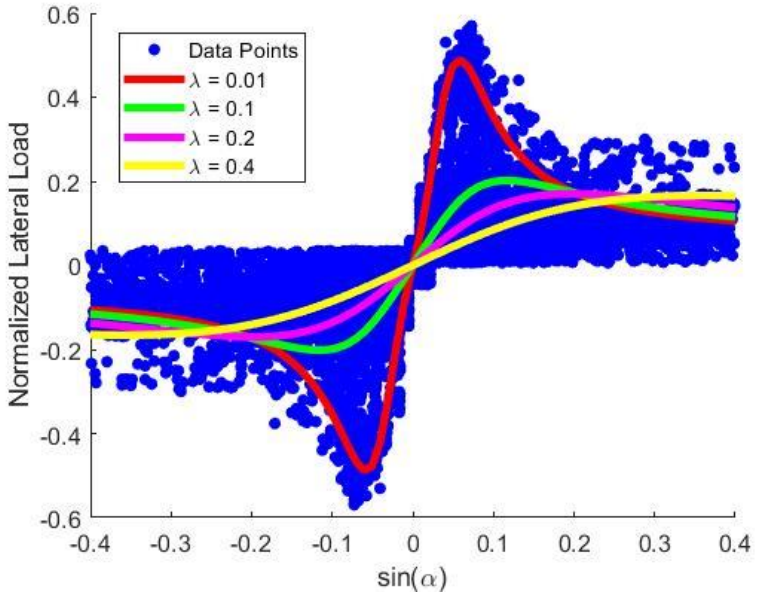

Figure 3.9 COMBINATOR Model in Lateral Direction

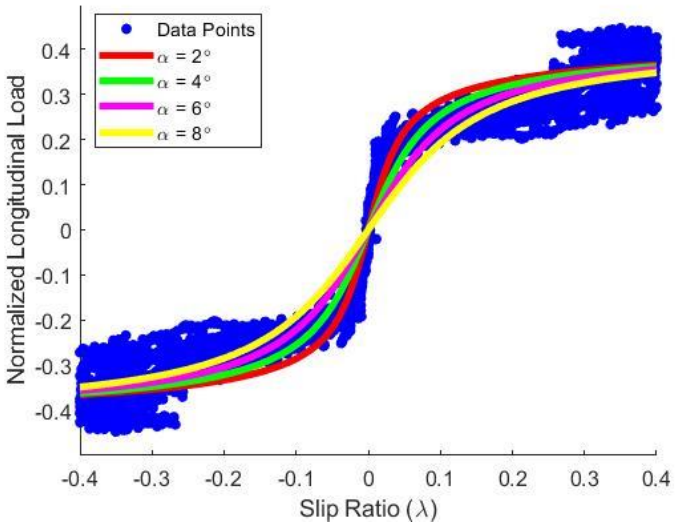

Figure 3.10 State Stiffness Model in Longitudinal Direction

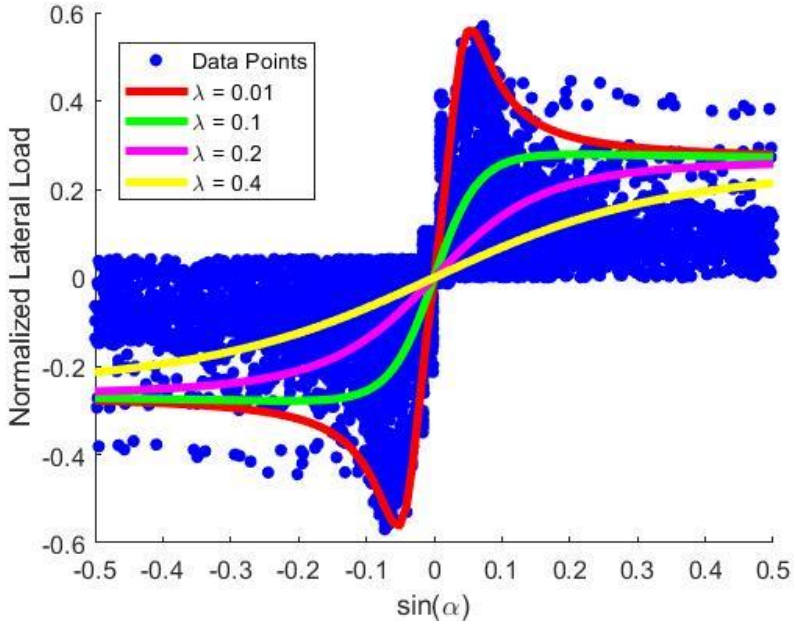

Figure 3.11 State Stiffness Model in Lateral Direction

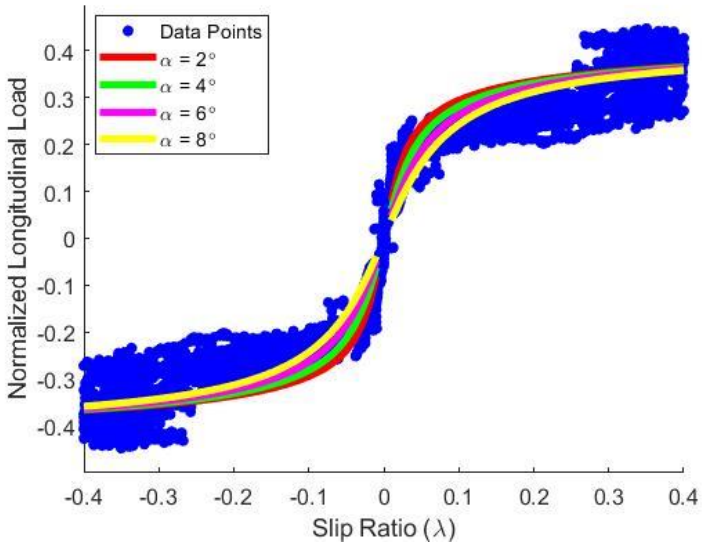

Figure 3.12 ADAMS Model in Longitudinal Direction

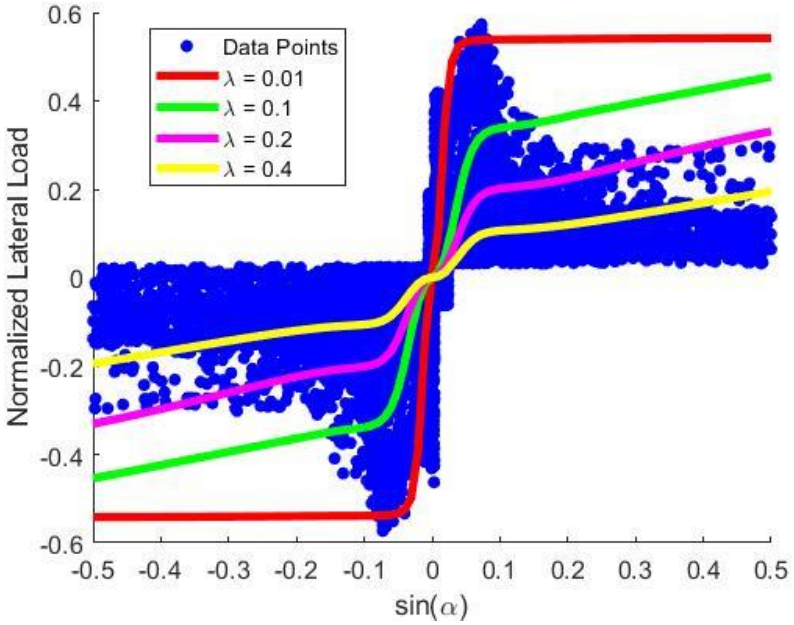

Figure 3.13 ADAMS Model in Lateral Direction

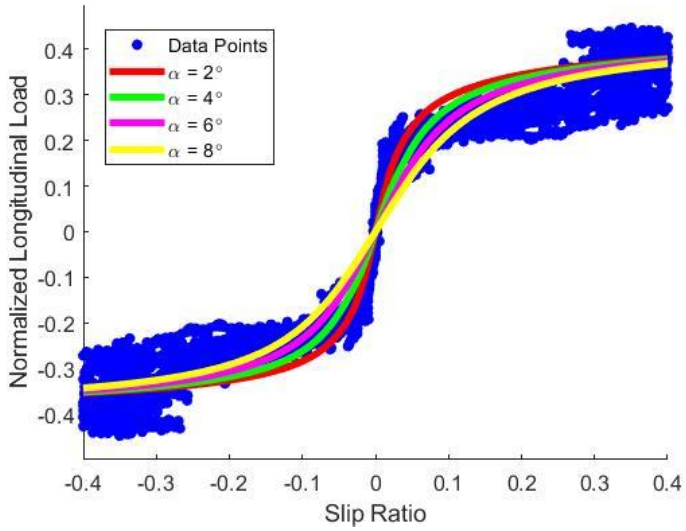

Figure 3.14 Region Invariant Slip Model in Longitudinal Direction

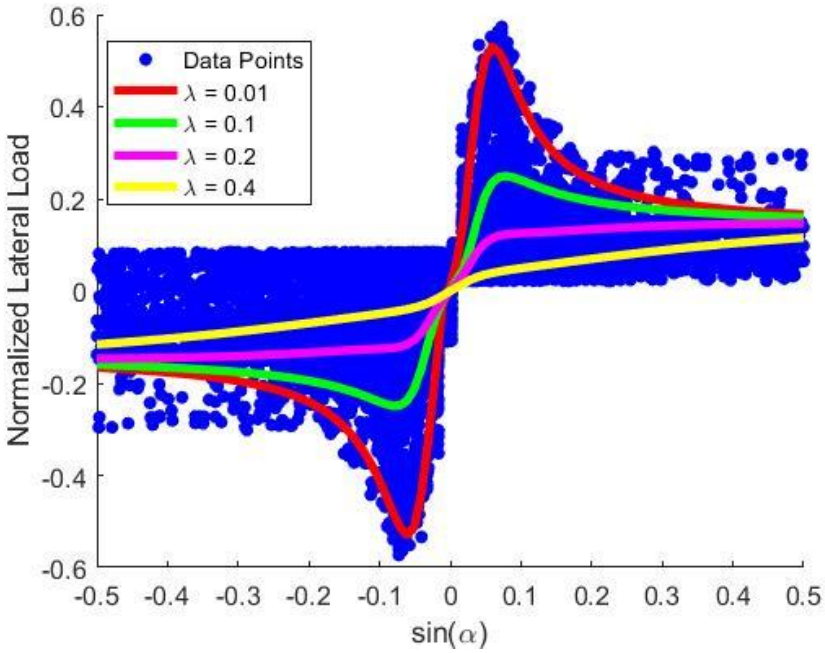

Figure 3.15 Region Invariant Slip Model in Lateral Direction

According to Table 3.1, these combined slip tire models vary significantly when compared with driving data. The figures indicate the behavior of each tire model deviates from data points in the sliding region. This contributed as the primary source of the errors in Table 3.1. Most combined slip tire force models are intended for use in the adhesion region because full steering control is maintained in the adhesion region. As indicated by Brach, modelling combined slip tire forces in the sliding region is difficult due to the nonlinear nature of dry friction behaviors in this region [86].

From Figure 3.9, it can be seen the COMBINATOR model does not agree well with the combined slip characteristics of the friction circle in the longitudinal direction. The friction circle indicates that the maximum longitudinal load should decrease as the sideslip angle increases however, the plot shows the maximum longitudinal load increased with sideslip angle between the 2° sideslip angle curve and the 4° sideslip angle curve. This could be due to the tire size of the Toyota Prius being smaller than those tested in the study of the COMBINATOR

by Pottinger, Pelz and Falciola [36]. Figures 3.13 and 3.14 indicate The ADAMS model became singular in the longitudinal and lateral directions at small slip ratios. The singular behavior may not make the ADAMS model suitable for slow driving scenarios.

This study has demonstrated that the State Stiffness model and the Region Invariant Slip model were the most accurate combined tire slip models. One could attribute the accuracy of these models to their foundation. The physical intuition of the brush model helped to derive relationships that is consistent with realistic combined tire slip loading behavior. Additionally, their generality allows these tire models to be applicable to various road conditions. This implies the brush model is a good representation of tires and that it is an effective tool for producing combined slip tire force models. Since the state stiffness model was the most accurate, this model was incorporated into the high-fidelity model.

3.5 Suspension Kinematics Modelling

The SEK joint can be used to develop reduced order suspension K&C models by replacing complicated suspension geometry with a set of constraints [55]. These constraints relate the position of automobile wheels with its chassis, to characterize relatice changes in wheel position and orientation. An advantage of the SEK joint is the elimination of the suspension geometry. Suspension links have negligible inertial properties, so their dynamics have little influence on suspension behavior. Hall presented two formulations of the SEK joint where one of them results in a set of Differential Algebraic Equations (DAEs) and the other generates Ordinary Differential Equations (ODEs). Only the ODE formulation was considered in this work because it was shown to reduce computational intensity [55]. Furthermore, only suspension kinematics was considered here because experimental data could not be generated for suspension compliance.

The ODE formulation of the SEK joint relies on curve fitting the relative motion between two bodies (see Figure 3.17). Specifically, the relative position must be expressed parametrically and in terms of arc length [55]. Curve fits for the relative Euler angles between the rigid bodies are also required if rotational motion is being considered. Curve fitting can be accomplished with parametric spline functions [90, 91] applied to data sets. Next, the parametric functions

are combined with a Frenet-Serret frame [56]. From a multibody dynamics perspective, the joint spaces and reaction spaces of the SEK joint are listed in Table 3.2.

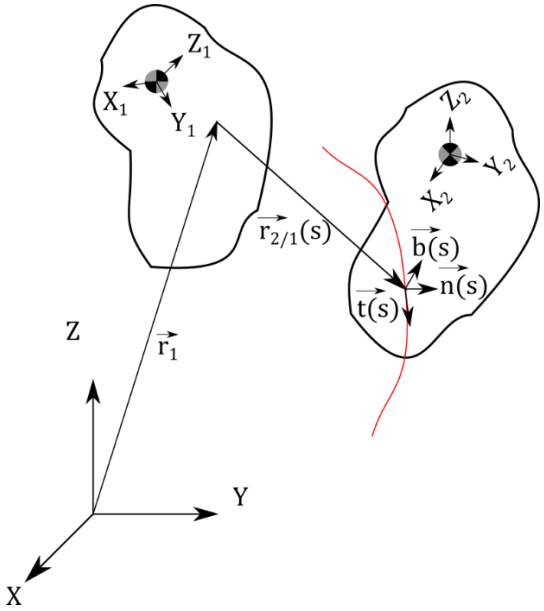

Figure 3.16 SEK Joint Principle

Table 3.2 Motion Spaces and Reaction Spaces of SEK Joint

Translational Motion Space	Translational Reaction Space	Rotational Motion Space	Rotational Reaction Space
$\vec{t}(s)$	$\vec{n}(s)\ and\ \vec{b}(s)$	$\emptyset$	$\mathbb{R}^3$

The Frenet-Serret frame is referenced by the tangential direction, $\vec{t}(s)$, the normal direction, $\vec{n}(s)$ and the binormal direction, $\vec{b}(s)$. Each of them are functions of the arc length parameter, s. It is important to recognize that the translational motion space is the tangential direction because the desired relative motion should be along the reference paths. Consequently, the constraint forces would be imparted by the reaction spaces which are the normal and binormal directions, respectively. According to Hall [55], the rotational motion space of the SEK joint

is empty set, $\emptyset$. Thus, rotational reaction moments will exist in $\mathbb{R}^3$. One may question how the rotational motion characterized by the Euler angles is enforced by the SEK joint if the rotational motion space is empty. Hall proposed a workaround where moments that induce rotational motion are converted into equivalent forces [55]. The equivalent forces are called torque projection forces and are derived from notions of generalized forces from Lagrangian mechanics [56]. For a given set of Euler angles and a resultant reaction moment, the torque projection force is defined by

$$F_{TP} = \vec{T}_{net} \cdot \frac{d\vec{\theta}}{ds}(s) \tag{3.23}$$

where $F_{TP} \in \mathbb{R}^3$ is the torque projection force, $\vec{T}_{net} \in \mathbb{R}^3$ is the resultant reaction torque and $\vec{\theta} \in \mathbb{R}^3$ is the vector of Euler angles.

3.5.1 Generating Suspension Kinematic Data

Suspension kinematic data for the Prius was generated using the wheel dolly (Figure 3.3), the VMS (Figure 3.1), and a hydraulic jack. A wheel of the Prius was carefully centered on the black pad of the wheel dolly (Figure 3.18) and a hydraulic jack was used to raise the vehicle off the dolly. The Prius was raised until the wheel and chassis started to move in unison.

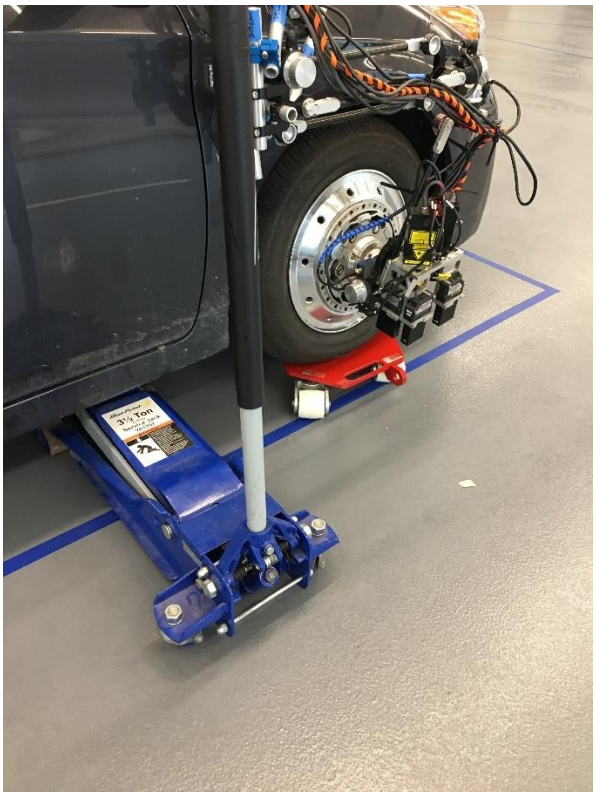

Figure 3.17 SEK Joint Testing

At this point, changes to a wheel's lateral and longitudinal displacement and orientation were no longer caused by suspension kinematics. Rather, the motion was merely excited by the hydraulic jack. Following this change, the vehicle was slowly lowered onto the wheel dolly. This process was repeated on all four wheels of the Prius and their motion profiles were recorded through the VMS. Figure 3.19 shows the lateral position of a wheel relative to its vertical position. Based on the coordinate system of the VMS, the wheel is moving inwards towards the chassis as the chassis was raised using the jack. At roughly 785mm of the vertical position, the wheel began to move in unison with the chassis, so the Prius was lowered onto the dolly again.

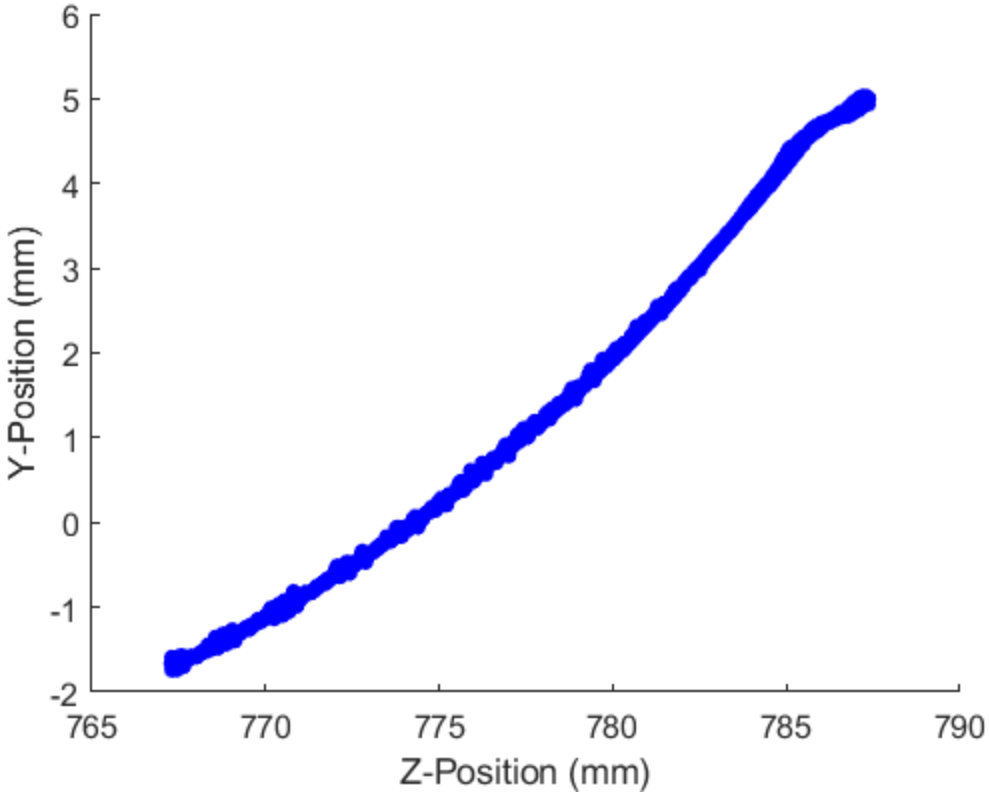

Figure 3.18 Lateral Position of Tire

The wheel dolly allows for reduced horizontal reaction forces between a ground surface and the tires. This alleviated an issue in data generation produced in a similar fashion [92]. Van Gennip performed the same procedure without a dolly and noticed that there was a hysteresis loss between the ascending and descending motions of the wheel. The introduction of the wheel dolly established symmetry between the two motions, yielding data appropriate for curve fits. Data was collected for all six degrees of freedom of a tire however, toe was treated as a constant in the SEK joint formulation. This was due to the toe angle experiencing negligible changes due to the suspension kinematics when performing the SEK joint test. The toe angle changed when the wheel moved in tandem with the chassis making that part of the data ineligible for use.

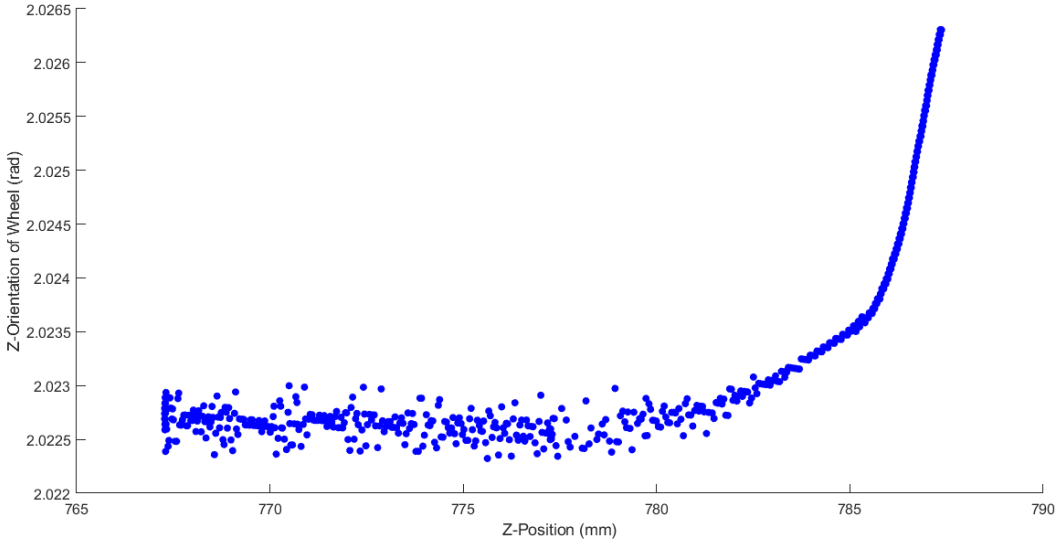

Figure 3.19 Wheel Orientation About SAE Z-Axis

3.5.2 Curve Fitting the Suspension Kinematic Data

The ODE formulation of the SEK joint requires fitting a parametric function to the wheel's displacement and orientation variables [55]. Hall suggested using B-splines for the curve fits because they can grant at least C^2continuity thereby allowing them to be paired with Frenet-Serret frames. B-splines were first introduced by de Boor as a parametric approach to curve fitting that minimized oscillations and established higher order continuity [90]. The general expression for a B-spline is

$$N(s) = \sum_{i=0}^{L} P_i B_{i,n}(s) \tag{3.22}$$

where $N \in R^3$ is a parametric vector function of parameter s, the $P_i \in \mathbb{R}^3$ are called control points and the $B_{i,n} \in \mathbb{R}^3$ are basis polynomials. The order of the basis polynomials is defined by n and L denotes the number of curve segments. Lines connecting the control points generate a convex polygon that confines the generated curve [93, 90, 91]. Therefore, the control points may not be on the curve. Constructing the basis polynomials requires identifying intermediate

values for s which locate points that the generated curve will pass through. These parameter values are commonly called knots and they can be expressed as a vector. For a given knot vector $p = [s_1, s_2, \dots, s_m]^T$ arranged in an increasing sequence, the basis polynomials can be computed recursively as

$$B_{i,0} = \begin{cases} 1, & s_i < s < s_{i+1} \\ 0, & otherwise \end{cases}$$

$$B_{i,j}(s) = \frac{s - s_i}{s_{i+j} - s_i} B_{i,j-1}(s) + \frac{s_{i+j+1} - s}{s_{i+j+1} - s_{i+1}} B_{i+1,j-1}(s) \tag{3.23}$$

The goodness of fit is influenced by the choice of knot locations and the number of knots. Unfortunately, determining the number of required knots and their locations are difficult problems to solve due to the large number of solutions [91]. The most popular solution was an iterative technique proposed by Tao and Watson [91]. Knots are added iteratively until a stopping condition is met. For a given knot added to the knot vector, an optimization algorithm is solved to position the knot such that the error between the spline, evaluated at the knot, and the data points are minimized. Knots are successively added in this manner until a goodness of fit measure begins to exhibit minimal changes.

Once a knot vector is found, the basis polynomials can be constructed, and the next step is to locate the control points. Considering that a B-spline lies in the convex polygon formed by connecting control points, a least-squares optimization process could be used to locate the control points.

$$J(P) = [x - N(s)]^T [x - N(s)] \tag{3.26}$$

Where $J \in \mathbb{R}$ is the cost function and $x \in \mathbb{R}^3$ is a data point. The cost function seeks to minimize the difference between the B-spline and the data points by suitably positioning the control points. Evaluating a B-spline using (3.24) is not practical. Rather, B-splines are commonly converted into piecewise polynomial functions with desirable continuity between segments [93].

Figures 3.21 to 3.24 show B-splines fitted to displacement and orientation data from the Prius as collected by the VMS. Displacements were selected for the translational variables so that the positions can be easily resolved with respect to other reference frames (i.e. center of mass of a vehicle).

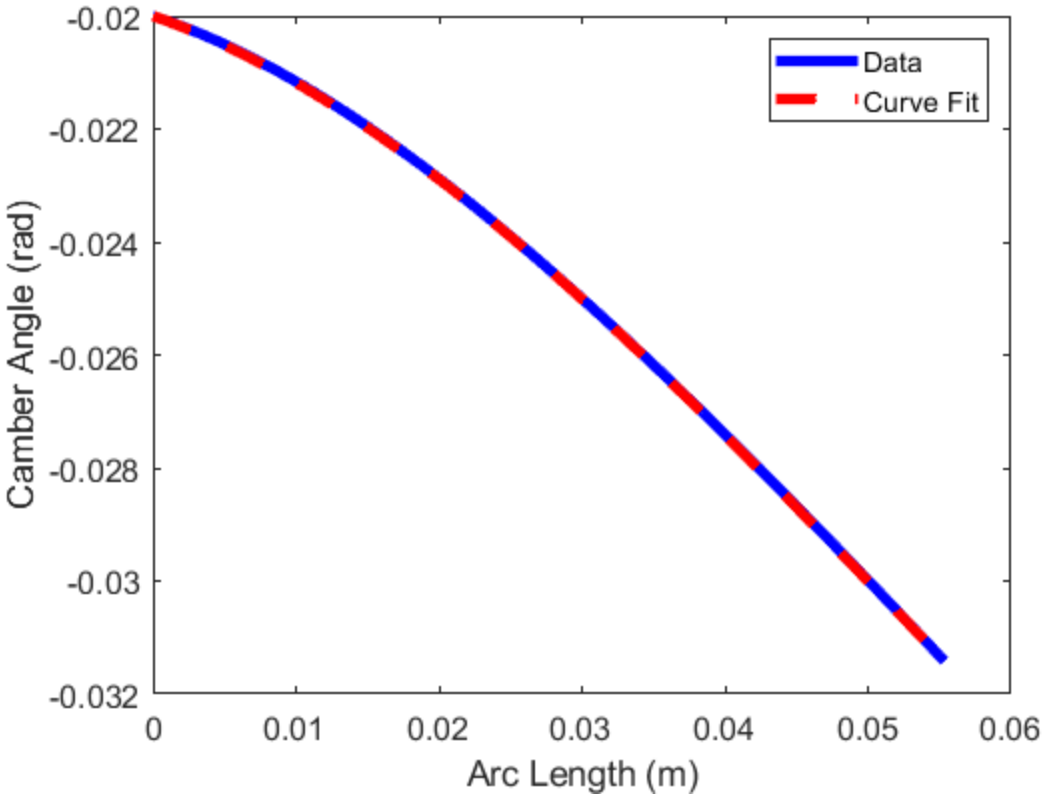

Figure 3.20 Camber Angle Profile

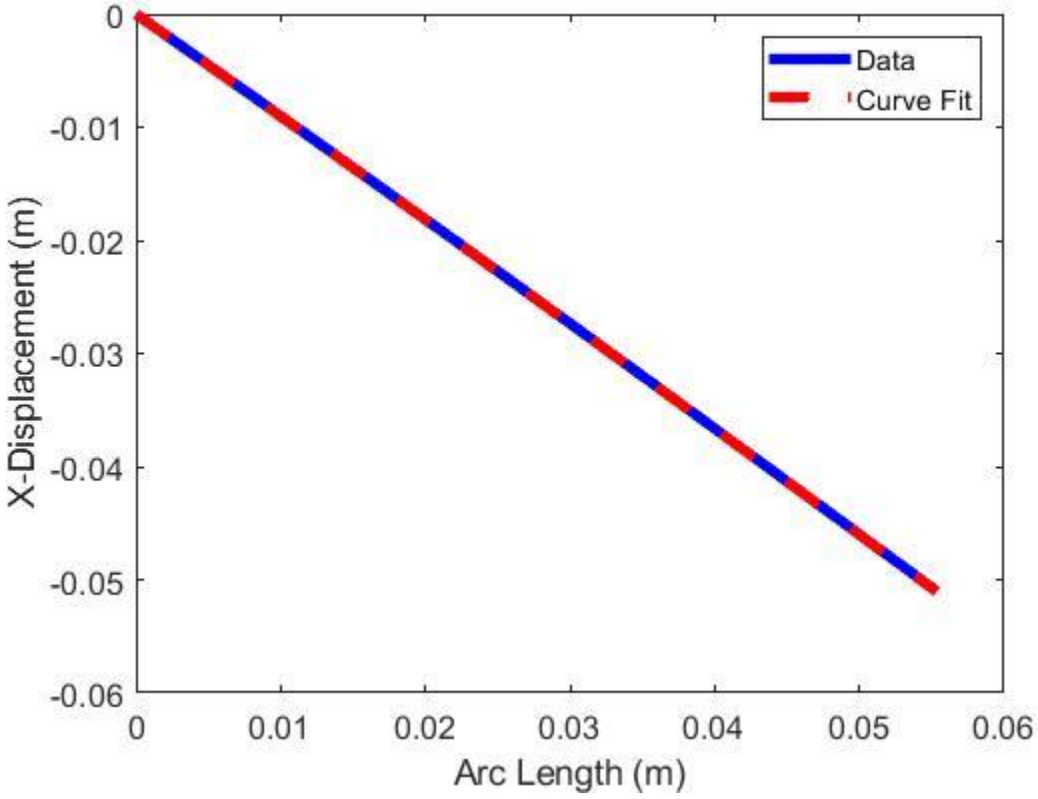

Figure 3.21 X-Displacement of Wheel

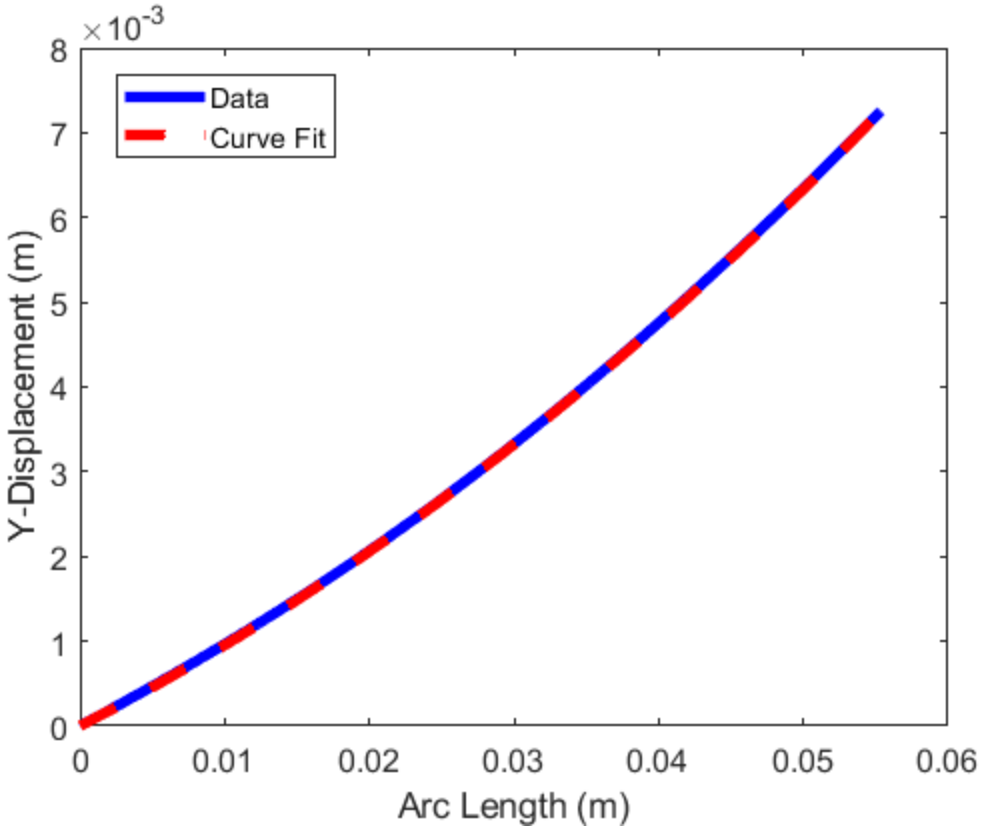

Figure 3.22 Y-Displacement of Wheel

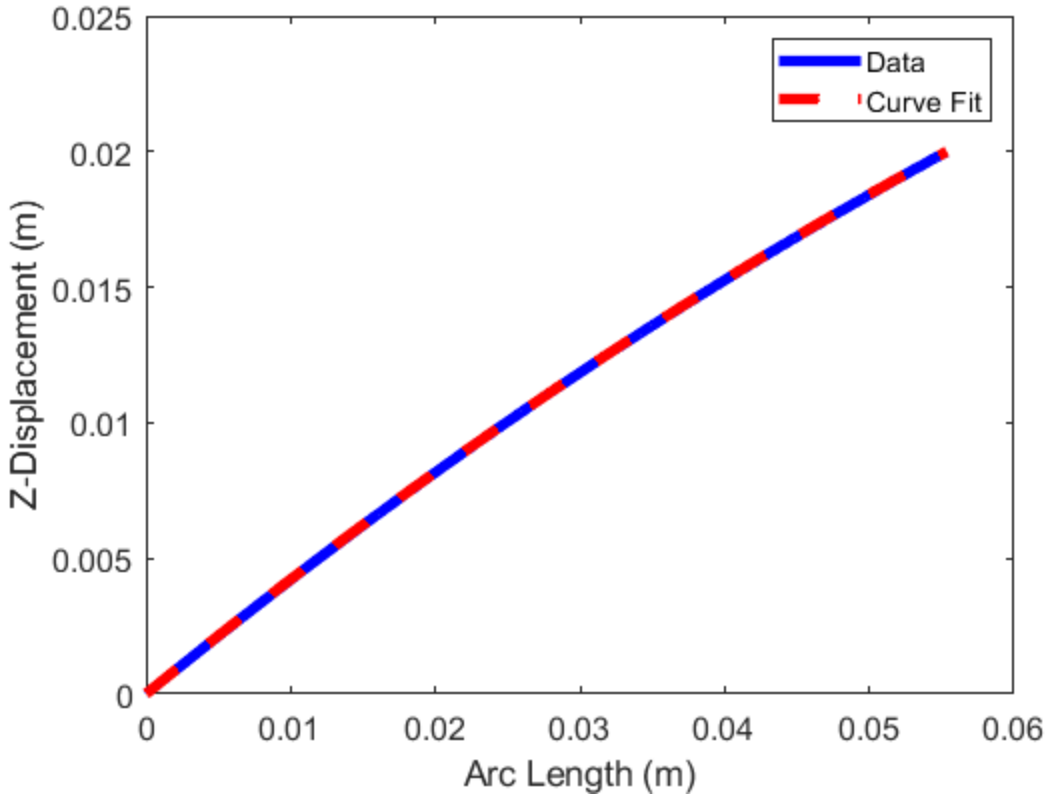

Figure 3.23 Z-Displacement of Wheel

3.5.3 Implementation of the SEK Joint

The high fidelity Prius model relies on prismatic joints to simulate suspension travel [15]. This means the wheels and chassis can only move vertically relative to each other. To apply the SEK joint, the suspension geometry of the Prius model must be altered. We first replace the prismatic joints with translational spring and damper components. Next, we resolve the relative displacement components from the curve fits above to an appropriate reference frame. For simplicity, the displacement components of the wheel can be converted to positions relative to the vehicle's center of mass. Before the SEK joint can be added to the model, the issue of wheel spin axis must be addressed. Revolute joints cannot be connected directly to the tire body because the camber angle changes. Consequently, this means the joint axes of the

revolute joints would also change. To resolve this issue, a small rigid body mass is added between the vehicle center of mass and the tire. Physically, this rigid body mass represents a wheel hub assembly [48]. Revolute joints can then be connected between the wheel hubs and tires to create revolute joints with a "variable" joint axis. Finally, the SEK joint can be connected between the vehicle center of mass and the wheel hubs. The MapleSim implementation of the new suspension architecture for a corner of the Prius is shown in Figure 3.25.

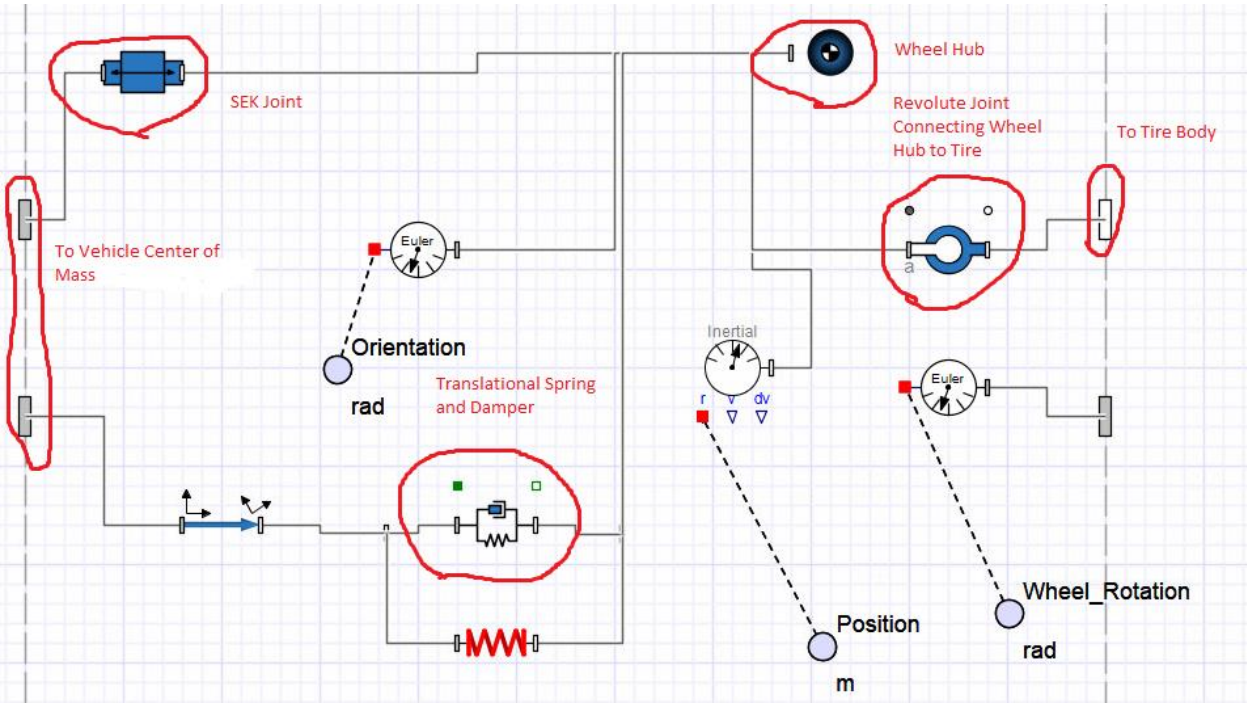

Figure 3.24 SEK Joint Implementation for Automobile Suspension on MapleSim

To make the suspension architecture consistent with a particular vehicle, new suspension parameters may need to be estimated. This is due to the presence of the SEK joint. The addition of the SEK joint means wheel travel is no longer in one direction akin to a prismatic joint. Therefore, parameters estimated using common two degree of freedom suspension models (i.e quarter-car suspension models or half-car suspension models) are no longer valid. Although not covered in this thesis, the parameters that would need to be estimated are:

- The Spring Stiffness
- The Damping Coefficient
- The Unstretched Length of the Spring-Damper Component
- The Inertial Parameters of the Wheel Hub

With a combined slip tire force model and suspension kinematics model added to the high-fidelity Prius model, the Prius model is prepared for controller testing on roundabouts. The added modelling components ensure that the Prius model can reflect realistic turning physics. Through the tires, the handling properties of a vehicle are defined. The SEK joint suspension model ensures the correct roll motion and wheel kinematic characteristics are reproduced. This is necessary to evaluate the roll characteristics of the high fidelity model under the influence of the path following controller. Although the implementation is presented here, the parameter estimation was not performed in this work so prismatic joints were used to the suspension system of the high fidelity model.

Chapter 4
Path Following

4.1 Path Following Controller Architecture

In this chapter, the development of a path following controller for roundabout navigation is presented. The problem of generating a reference path for the Prius is first discussed. Then, an upper level controller is presented using a kinematic path following algorithm. The following sections show a modification of the algorithm to adapt it for roundabout paths. Following the design of the upper level controller, an actuator controller is presented which physically fulfills the commands of the upper level controller. A flowchart of the control system is presented in Figure 4.1.

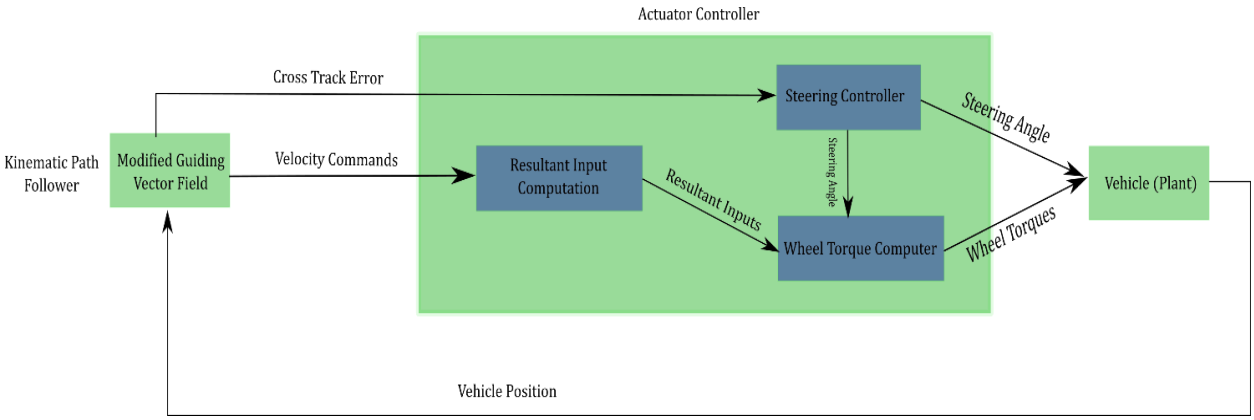

Figure 4.1 Path Following Control System Block Diagram

4.2 Path Generation for Roundabouts

When making reference paths for roundabout navigation, Gonzalez argued for the use of spline interpolation functions [94]. Specifically, Bézier curves were recommended as a suitable spline function for these paths. Bézier curves [95, 94, 96] are parametric splines, with curve parameter $\beta \in [0,1]$, defined by the general expression

$$W(\beta) = \sum_{i=0}^{z} \binom{z}{i} (1-\beta)^{z-i} \beta^{i} P_i \tag{24}$$

where $W \in \mathbb{R}^n$ and z is the order of the spline. The P_i are points in $\mathbb{R}^n$ and are referred to as control points because they influence the shape of a Bézier curve. The control points may not necessarily be on the curve. Rather, the Bézier curve lies within the convex hull formed by the control points [96]. These points can be optimally placed by minimizing curvature thereby reducing unwanted oscillations in path generation. This feature makes Bézier curves attractive for path planning algorithms [95]. Moreover, Bézier curves promote low computational costs and paths that can lead to comfortable driving scenarios. Gonzalez et al. further states that this optimization process allows one to define smooth entry and exit paths that seem natural for roundabout navigation [94]. As an example, consider a straight drive-through motion on a roundabout, as shown in figure 4.2.

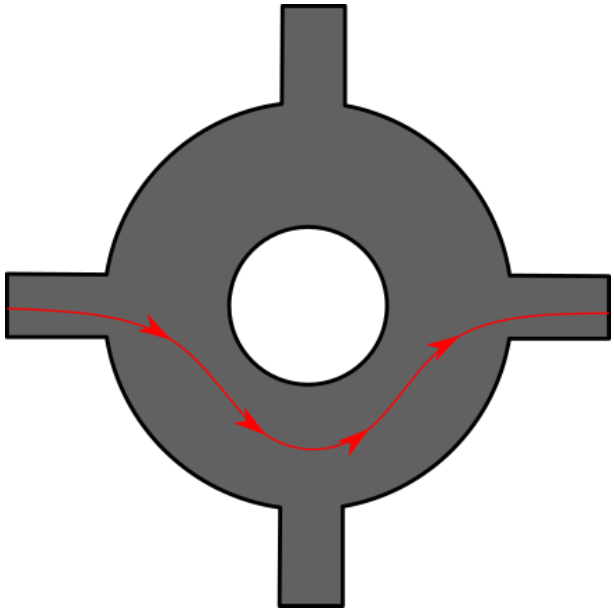

Figure 4.2 Roundabout with Straight Drive Through Path

A vehicle enters and exits a roundabout at opposite ends. The reference path can be defined by three curve segments with at least C^1continuity between them. The first segment defines

the entry path for the vehicle, the second segment is the circular part of the roundabout and the third segment represents the exit path. Following the approach inspired by Gonzalez et al [94], the entry and exit paths were defined by cubic Bézier curves and the circular portion was defined using the parametric equation for a circle

$$q(\theta) = Rcos(\theta)\hat{\imath} + Rsin(\theta)\hat{\jmath} \tag{4.3}$$

where $q \in \mathbb{R}^2$, $\theta \in [0,2\pi)$ and R is the radius of the circle. The cost function was defined as

$$J = \kappa(\beta_0) + \kappa(\beta_1)$$

$$\kappa(\beta) = \frac{\left\| \frac{dW}{d\beta} \times \frac{d^2W}{d\beta^2} \right\|}{\left\| \frac{dW}{d\beta} \right\|^3} \tag{4.4}$$

where $\kappa \in \mathbb{R}$ is the curvature of the path [56]. Evaluating the curvature at $\beta = 0$ and $\beta = 1$, respectively, resulted in the curvature being expressed in terms of the control points. Next, boundary constraints were imposed. The boundary constraints ensured that the generated reference path had no inflections and was natural for roundabout navigation. Figure 4.3 shows a physical depiction of the constraints.

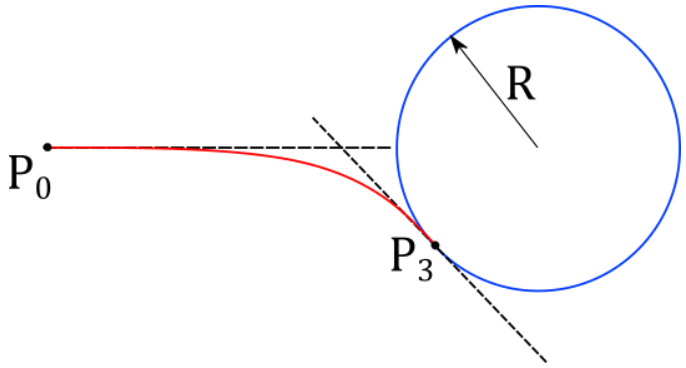

Figure 4.3 Constraint Derivation for Roundabout Paths

A vehicle was assumed to approach the entry path in a straight line at a known point, P_0. This implies one of the constraint boundaries is a straight horizontal line at P_0. Next, the vehicle was assumed to merge into the circular portion of the roundabout at a known point, P_3. This led to the other constraint boundary being a line tangent to the roundabout circle at P_3. Given coordinates x and y in $\mathbb{R}^2$, the boundary constraints were expressed as

$$\begin{aligned} y &\leq 0 \\ y - mx &\leq b \end{aligned} \tag{4.5}$$

where m is the slope of the line tangent to the circle at P_3 and b is the y-intercept of the tangent line. These quantities can be computed by evaluating the derivative of (4.3) with respect to θ at the merge point, P_3. Applying these two constraints, ensured that the generated path was similar to the red curve in Figure 4.3. Expressing the constraints in terms of the decision variables, $P_1 \in \mathbb{R}^2$ and $P_2 \in \mathbb{R}^2$, resulted in

$$AP \leq d$$

$$A = \begin{bmatrix} 0 & 1 & 0 & 0 \\ 0 & 0 & 0 & 1 \\ -m & 1 & 0 & 0 \\ 0 & 0 & -m & 1 \end{bmatrix}, \qquad P = \begin{bmatrix} P_{1_x} \\ P_{1_y} \\ P_{2_x} \\ P_{2_y} \end{bmatrix}, \qquad d = \begin{bmatrix} 0 \\ 0 \\ b \\ b \end{bmatrix} \tag{4.6}$$

The optimization problem with cost function (4.4) and constraints (4.6) was solved using MATLAB's *fmincon* command [97] for a 15m radius roundabout. The resulting path is shown in Figure 4.4 and the control points of the entry path are listed in Table 4.1. The exit path was assumed to be symmetrical to the entry path therefore each set of coordinates in Table 4.1 were reflected about the global X-axis. It should be noted that lanes were not considered in path generation to maintain generality for path generation and for consideration with various types of roundabouts.

Table 4.1 Roundabout Entry Control Points

	P_0	P_1	P_2	P_3
Coordinates	(-40,0)	(-20.20,0)	(-15.53,-5.67)	(-10.60,-10.60)

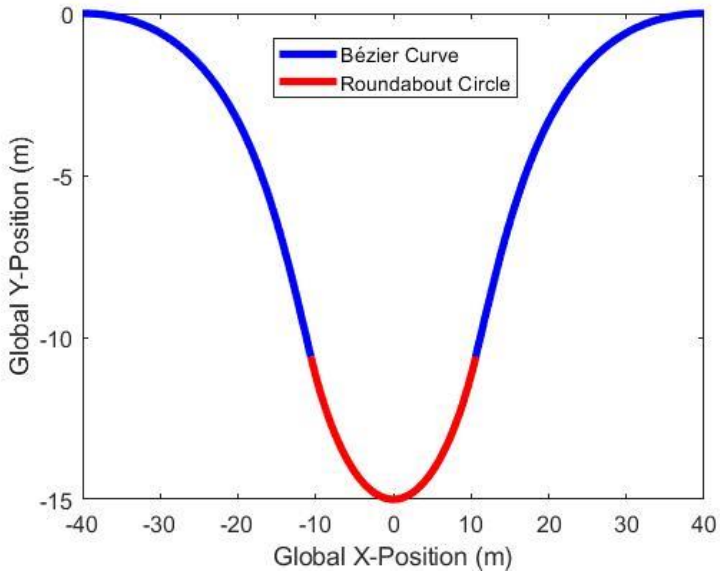

Figure 4.4 Roundabout Reference Path

It should be noted that the merge point, P_3 was selected through a trial and error process. Referring to Figure 4.3, if the merge point was closer to the left of the circle, then the resulting path would have been sharper. This means the Prius would enter and exit the roundabout in an aggressive manner. To avoid this, a point closer to the bottom of the circle was chosen thereby requiring a gradual steering motion from the Prius.

4.3 Guiding Vector Field

A vector field path following algorithm called the Guiding Vector Field (GVF) algorithm was proposed for navigating ground vehicles [63]. This algorithm defines a velocity vector field that assigns a velocity and an orientation for a vehicle to take based on its position. It was shown, mathematically and through application, that the GVF leads to globally asymptotically stable convergence to reference paths. Furthermore, the vector field becomes tangential to a

reference path if a vehicle is on the path allowing the vehicle to traverse the path without deviating from it. When compared to the LOS and NLGL algorithms, the guiding vector field was shown to perform better than them [63].

Creating the vector field requires expressing a reference path as a contour map. In general, it may not be possible to represent a reference path as a contour map. Reference paths defined using parametric functions, for example, are ineligible functions for the GVF algorithm because parametric functions cannot be converted to functions in Cartesian coordinates. However, Gonzales et al. mentioned parametric functions are frequently used in path planning algorithms [95, 94]. Moreover, Rubi et al. also indicated that underwater vehicles and ground robots pair path planners with path following strategies [57]. Developing path following strategies that could be used with parametric path planners for autonomous vehicle navigation would provide the benefits that Rubi et al. mentioned are associated with path following.

To apply the GVF algorithm to roundabouts, the algorithm must be modified for use with parametric functions. Typically, control theoretic approaches are used for path following with parametric functions. One attaches a moving frame onto a reference path with its own controllable kinematics and then impose control laws to influence the motion of vehicles and the moving frames [98, 99, 100, 101, 102]. Although stronger robustness and greater flexibility in path following is provided through control theoretic approaches, Sujit et al. and Rubi et al. indicate control theoretic algorithms are more difficult to implement on physical systems, require greater tuning effort, and are more computationally laborious than the geometric methods [57, 58].

4.4 The Dual Space and One-Forms

For any vector space V, there is a co-existing vector space called the dual space denoted by V^* [103]. The dual space is defined as the set of all linear functionals, L, that act on the vector space. That is,

$$V^* \triangleq L(V, \mathbb{R}) \tag{4.7}$$

The dimension of a dual space is the same as that of its associated vector space and elements of a dual space are called co-vectors or one-forms [103]. Let V be an n-dimensional vector space, over $\mathbb{R}$, with basis $\{g_1, g_2, \dots, g_n\}$. There exists a basis, $\{g^1, g^2, \dots, g^n\}$ for V^*, the dual basis, that satisfies property (4.8), where δ_j^i is the Kronecker delta function [104].

$$g^i(g_j) = \delta_j^i \tag{4.8}$$

Consider a one-form $\phi \in V^*$. The dual basis can be used to express ϕ in terms of vector components $[a_1, a_2, \dots, a_n]$ where $a_i \in \mathbb{R}$.

$$\phi = \sum_{i=1}^{n} a_i g^i \tag{4.9}$$

For a vector, $x \in V$ with components $[x_1, x_2, \dots, x_n]$, where $x_i \in \mathbb{R}$, a one–form, ϕ evaluated on a vector can be computed algebraically as

$$\phi(x) = \sum_{i=1}^{n} a_i x_i \tag{4.10}$$

While vectors can be visually depicted as arrows, one-forms can be visually represented as contours of functions in $\mathbb{R}^{n-1}$ (see Figure 4.5) [105].

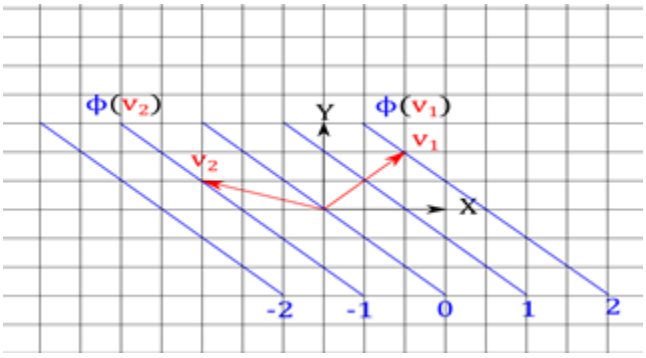

Figure 4.5 A Visual Depiction of the One-Form $\boldsymbol{\phi = g^2 + g^1 \in \mathbb{R}^{2^*}}$

The level sets of the contour map correspond to specific outputs of the one–form for vectors extending from an origin. The numerical output of a one-form, for a vector input, can be

visually interpreted as the number of contours the vector pierces. The sign of the output depends on the direction of the vector and of the one-form. If the vector, points in the direction of increasing contours, the result is positive. Otherwise, the result is negative. Further details on the dual space and one–forms can be found in [103, 105, 106, 104].

4.5 Modified Guiding Vector Field Algorithm

Given a smooth parametric function $P: I \rightarrow D$, where $I \subset \mathbb{R}$ and $D \subset \mathbb{R}^2$ and assuming a vehicle's position can be described by a vector in $\mathbb{R}^2$, a one-form can be used to establish an explicit relationship between a vehicle's location and a curve parameter, $\beta \in I$.

4.5.1 Relating a Vehicle's Position to a Curve Parameter

To build the required one-form, we construct a secant line, in Cartesian coordinates, connecting the endpoints of the reference path. This secant line is referred to as the parameter indexing line (PIL). Next, we find the slope of a line perpendicular to the PIL. The perpendicular slope will then be used to make the one–form

$$\alpha = g^2 + mg^1 \tag{4.11}$$

where m is the perpendicular slope to the PIL and the g^i are the standard dual basis on $\mathbb{R}^{2*}$. Visually depicting (34) shows it produces a contour map of lines perpendicular to the PIL (see Fig. 2). Because $\alpha: \mathbb{R}^2 \rightarrow \mathbb{R}$, a vehicle position vector, $r_v \in \mathbb{R}^2$, can be passed as an argument to (4.11). Therefore, a vehicle must always lie on a perpendicular contour in $\mathbb{R}^2$ meaning the output of $\alpha(r_v)$ can be related to a curve parameter, β.

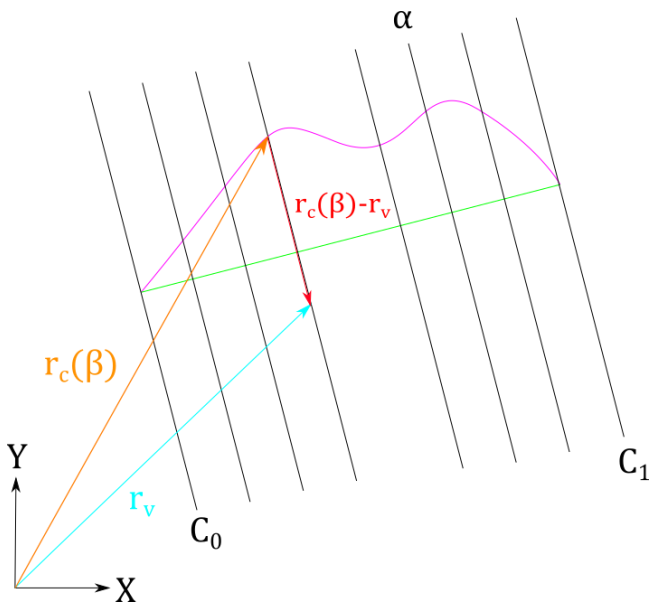

Figure 4.6 The Relationship Between Points on a Curve and a Vehicle's Coordinates

Generally, parametric curves have parameters with restricted domains. Notably, parametric curves used to create spline functions [95, 94, 96]. For these types of curves, $\beta \in I$, where $I \subset \mathbb{R}$. Assigning the output of (6) for a vehicle position as the curve parameter will cause the parameter to assume infeasible values because the one-form is defined on all of $\mathbb{R}^2$. We resolve this issue as follows. Consider a parametric function with position vector $r_c(\beta) \in \mathbb{R}^2$, defined by parameter $\beta \in I$ where $I \triangleq [\beta_0, \beta_1] \subset \mathbb{R}$. We observe that the position vector, r_c can also be passed as an argument to (4.11) for all admissible values of β (see Figure 4.6). Evaluating (4.11) at the endpoints of the curve give us two scalars, $C_0, C_1 \in \mathbb{R}$.

$$C_0 = \alpha\big(r_c(\beta_0)\big), \qquad C_1 = \alpha(r_c(\beta_1)) \tag{4.12}$$

Let $r_v \in \mathbb{R}^2$ be the position vector of a vehicle. We propose the curve parameter can be obtained from a vehicle's position by using the linear function

$$\beta = G(\alpha(r_v) - C_0) + \beta_0, \qquad G = \frac{\beta_1 - \beta_0}{C_1 - C_0} \tag{4.13}$$

Although (4.13) is defined over all $\mathbb{R}^2$, the domain of (4.13) should be restricted to a subset of $\mathbb{R}^2$ so that β could assume admissible values in I. Consider a vehicle's position expressed in terms of an inertial frame in Cartesian coordinates. That is, $r_v = [x\ y]^T$. Let $S \triangleq \{(x,y) \in \mathbb{R}^2 : C_0 \leq \alpha\big(r_v(x,y)\big) \leq C_1\}$ then $\forall (x,y) \in S,\ \beta_0 \leq \beta \leq \beta_1$. Expressing a vehicle's position in terms of its coordinates and using (4.12) allows (4.11) and (4.13) to be written as

$$\alpha(x,y) = y + mx \tag{4.14}$$

$$\beta(x,y) = G(\alpha(x,y) - C_0) + \beta_0 \tag{4.15}$$

4.5.2 Changes to the Vector Field

We use the same form of expression for the guiding vector field from [63] but we propose changes to the elements that make the guiding vector field. The tangent and normal vector fields from the original definition are replaced with parametric expressions for tangent vectors, $t \in \mathbb{R}^2$ and normal vectors, $n \in \mathbb{R}^2$ to a curve based on a Frenet-Serret frame in two dimensions [56].

$$t(\beta) = \frac{dr_c}{d\beta} \tag{4.16}$$

$$n(\beta) = Et(\beta); \quad E = \begin{bmatrix} 0 & -1 \\ 1 & 0 \end{bmatrix} \tag{4.17}$$

Next, we propose replacing the error function in the original definition with the error function in (4.18).

$$e(\beta) = < r_{rel}, u_n(\beta) >, \qquad r_{rel}(\beta) = r_v - r_c(\beta) \tag{4.18}$$

Where $u_n \in \mathbb{R}^2$ is a unit normal on the path and $<\cdot,\cdot>$ denotes the standard inner product on $\mathbb{R}^2$. The error term, $e \in \mathbb{R}$, in (4.18) is called the cross – track error and it measures how far a

vehicle is orthogonally to a point on the reference path. Finally, by using (4.16), (4.17) and (4.18) and recognizing that a curve parameter can be related to a vehicle's location through (4.15), we can write the modified guiding vector field as

$$v\big(\beta(x,y)\big) = t\big(\beta(x,y)\big) - \rho e\big(\beta(x,y)\big) n(\beta(x,y)) \tag{4.19}$$

where $v: \mathbb{R}^2 \rightarrow \mathbb{R}^2$ and $\rho \geq 0$ is a tunable gain that affects the convergence rate of a vehicle to the reference path. Increasing values of ρ make a reference path more attractive causing a vehicle to approach it more aggressively. In general, we remark that ρ need not be a constant but is treated as a constant for simplicity. Based on the definition in (4.19), if a vehicle approaches a reference path then $e(\beta) \rightarrow 0$ and consequently, $v(\beta) \rightarrow t(\beta)$ meaning the vector field would guide a vehicle tangentially along a path.

4.5.3 Using the Modified Guiding Vector Field

Generating translational velocity requirements that direct a vehicle to the reference path from the guiding vector field can be done using the same relationships in [63]. However, when computing them, the curve parameter map from (4.15) must be considered as well.

$$\dot{r_d} = U m_d\big(\beta(x,y)\big), \;\; m_d\big(\beta(x,y)\big) = \frac{v\big(\beta(x,y)\big)}{\big\|v\big(\beta(x,y)\big)\big\|} \tag{4.20}$$

Where $\dot{r_d} \in \mathbb{R}^2$ is the desired velocity in the x and y directions respectively, $U \in \mathbb{R}$ is a chosen longitudinal velocity for a vehicle to track and $m_d \in \mathbb{R}^2$ is the modified guiding vector field normalized into a unit vector field. Deriving a desired yaw rate from the modified approach, however, requires the chain rule due to the parameter map in (4.15). This fact makes the desired yaw rate in (4.21) different from the desired yaw rate presented in [63]. The desired rotation rate of a vehicle can be found as follows.

$$\omega_d = \dot{m}_d\big(\beta(x,y)\big) = \left(-\frac{dm_d\big(\beta(x,y)\big)}{d\beta}\left[\frac{d\beta}{d\alpha}\left(\frac{\partial\alpha}{\partial x}\dot{x}_d + \frac{\partial\alpha}{\partial y}\dot{y}_d\right)\right]\right) Em_d(\beta(x,y)) \qquad (4.21)$$

The additional term given by the derivatives of the parameter map and the one-form act as a scaling term. The derivative of m_d with respect to β can be computed by differentiating the relationship between the two in (4.20). Moreover, the derivatives $\frac{\partial\alpha}{\partial y}$, $\frac{\partial\alpha}{\partial x}$ and $\frac{d\beta}{d\alpha}$ can be computed from (4.14) and (4.15) respectively. It should be noted $\dot{x}_d$ and $\dot{y}_d$ are the desired translational velocity components from $\dot{r}_d$ in (4.20). Furthermore, the Em_d factor appears using E from (4.17), because $\|m_d\|_2 = 1$. Therefore $\dot{m}_d \perp m_d$ which implies that $\dot{m}_d$ is proportional to the unit vector Em_d. This means $\dot{m}_d = -\omega_d(\beta)Em_d(\beta)$ and therefore ω_d can be interpreted as the curvature of the integral curves generated by the modified guiding vector field.

4.5.4 Stability of the Modified Guiding Vector Field

We use Lyapunov's direct method [107] to show that the velocity vector field in (4.19) leads to asymptotically stable dy. Firstly, we recognize the guiding vector field in (4.19) satisfies the set of autonomous ordinary differential equations

$$\frac{d}{dt}r_v(t) = v(\beta\big(r_v(t)\big) \in \mathbb{R}^2 \qquad (4.22)$$

Let us define the Lyapunov function for the error dynamics as

$$V = \frac{1}{2}e\big(\beta(r_v)\big)^2 \qquad (4.23)$$

Differentiating (4.23) with respect to time gives

$$\dot{V} = e\big(\beta(r_v)\big)\,\dot{e}\big(\beta(r_v)\big) \qquad (25)$$

Differentiating (4.18) with respect to time gives

$$\dot{e}(\beta) = < \frac{d}{dt} r_{rel}(\beta), u_n(\beta) > + < r_{rel}(\beta), \frac{du_n}{dt} > \tag{4.25}$$

Since the chain rule is required, we can use (4.15) and (4.18) to find the time derivative of the relative position vector term in (4.26). We have suppressed the implicit relationship between β and the vehicle coordinates, from (4.15), for clarity.

$$\frac{d}{dt} r_{rel}(\beta) = v - t(\beta) \frac{\partial \beta}{\partial x} \dot{x}_d - t(\beta) \frac{\partial \beta}{\partial y} \dot{y}_d \tag{4.26}$$

Substituting (4.19) allows us to replace the first term in (4.26).

$$\frac{d}{dt} r_{rel}(\beta) = t(\beta) - \rho e(\beta) n(\beta) - t(\beta) \frac{\partial \beta}{\partial x} \dot{x}_d - t(\beta) \frac{\partial \beta}{\partial y} \dot{y}_d \tag{4.27}$$

Next, we differentiate the unit vector, $u_n(\beta)$ with respect to time using the chain rule. Assuming the coordinate frame attached to the reference path is right - handed, we can say that the derivative of $u_n(\beta)$ with respect to the curve parameter is equivalent to scaling a unit tangential vector, $u_t(\beta)$ along the reference path [56]. Therefore,

$$\frac{du_n}{d\beta} = k(\beta) u_t(\beta) \tag{4.28}$$

The scaling factor, $k(\beta) \in \mathbb{R}$ is known as the curvature of the path [56]. Relationship (4.28) can then be used to write the time derivative of the unit vector, $u_n(\beta)$ as

$$\frac{du_n}{dt} = \frac{du_n}{d\beta} \left(\frac{\partial \beta}{\partial x} \dot{x}_d + \frac{\partial \beta}{\partial y} \dot{y}_d \right), \tag{4.29}$$

$$\frac{du_n}{dt} = k(\beta) \left(\frac{\partial \beta}{\partial x} \dot{x}_d + \frac{\partial \beta}{\partial y} \dot{y}_d \right) u_t$$

Equations (4.27) and (4.29) can be used to re – write (4.25) as

$$\dot{e}(\beta) =< \left(t(\beta) - \rho e(\beta) n(\beta) - t(\beta)\frac{\partial \beta}{\partial x}\dot{x}_d - (\beta)\frac{\partial \beta}{\partial y}\dot{y}_d\right), u_n(\beta) > + \tag{4.30}$$

$$< \left(r_v - r_c(\beta)\right), k(\beta)\left(\frac{\partial \beta}{\partial x}\dot{x}_d + \frac{\partial \beta}{\partial y}\dot{y}_d\right) u_t(\beta) >$$

The first term can be considerably simplified by recognizing that $t(\beta) \perp u_n(\beta) \ \forall \beta \in I$ so $< t(\beta), u_n(\beta) >= 0$ and that $n(\beta) \parallel u_n(\beta) \ \forall \beta \in I$ meaning $< n(\beta), u_n(\beta) > \equiv \|n(\beta)\|_2$. Additionally, (4.15) can be differentiated to determine $\frac{\partial \beta}{\partial x}$ and $\frac{\partial \beta}{\partial y}$.

$$\dot{e}(\beta) = -\rho e(\beta)\|n(\beta)\|_2 + < r_{rel}(\beta), k(\beta)(Gm\dot{x}_d + G\dot{y}_d)u_t(\beta) > \tag{4.31}$$

Equation (4.31) can now be substituted into (4.24) to expand the time derivative of the Lyapunov function.

$$\dot{V} = -\rho e^2(\beta)\|n(\beta)\|_2 + < \left(r_{rel}(\beta), k(\beta)(Gm\dot{x}_d + G\dot{y}_d)u_t(\beta)\right)e(\beta) > \tag{4.32}$$

Note that, $k(\beta)(Gm\dot{x}_d + G\dot{y}_d)u_t(\beta)$ is a scaling along the unit tangential so we can re-write it as $b(t)u_t(\beta)$ where $b(t)$ is a time varying scalar. Focusing on the second term in (4.32) and using (4.18) to expand $e(\beta)$, we can re-write (4.32) as

$$\dot{V} = -\rho e^2(\beta)\|n(\beta)\|_2 + [< r_{rel}(\beta), b(t)u_t(\beta) >][< r_{rel}(\beta), u_n(\beta) >] \tag{4.33}$$

We now simplify the expression by invoking the projection angle property of the standard inner product: $< A, B >= \|A\|_2\|B\|_2 \cos(\theta)$ where $A,\ B \in \mathbb{R}^n$ and $\theta \in [0, \pi]$ is the angle between the two vectors A and B. Let θ be the angle between $r_{rel}(\beta)$ and $u_n(\beta)$. Since $u_t(\beta)$ is orthogonal to $u_n(\beta)$, the angle between $r_{rel}(\beta)$ and $u_t(\beta)$ must be $\theta + \frac{\pi}{2}$. Using these properties, (4.33) becomes

$$\dot{V} = -\rho e^2(\beta)\|n(\beta)\|_2 + \|r_{rel}(\beta)\|_2^2\|b(t)u_t(\beta)\|_2 \cos(\theta)\cos\left(\theta + \frac{\pi}{2}\right) \tag{4.34}$$

$$\dot{V} = = -\rho e^2(\beta)\|n(\beta)\|_2 - \|r_{rel}(\beta)\|_2^2\|b(t)u_t(\beta)\|_2 \sin(\theta)$$

The time derivative of the Lyapunov function in (4.34) is negative definite implying that the trajectories of (4.19) are asymptotically stable if $(x, y) \in S$. Therefore, a vehicle can merge

onto a parametric reference path using the modified MGVF if it is anywhere between the endpoints of the path.

4.5.5 Bézier Curve Example

An example construction of the modified guiding vector field on a planar Bézier curve is presented in Figure 4.7 with its control points listed in Table 4.2.

Table 4.2 Bézier Curve Control Points

	P_0	P_1	P_2	P_3
Coordinates	(0,0)	(3,7)	(5,3)	(10,5)

We find the slope of a line perpendicular to the PIL with endpoints (P_0 and P_3, respectively) for the curve in Fig. 3 and substitute it into (5). This gives the one-form

$$\alpha = g^2 + 2g^1 \tag{4.35}$$

Next, we evaluate the one-form (4.35) at the endpoints using (4.12) to get the scalars, C_0 and C_1.

$$C_0 = \alpha(P_0) = 0, \qquad C_1 = \alpha(P_1) = 25 \tag{4.36}$$

Finally, substituting (4.35) and (4.36) into (4.13) and then the result into (4.15) gives

$$\beta(x, y) = \frac{1}{25}(y + 2x) \tag{4.37}$$

where x and y are the coordinates of a vehicle's center of mass.

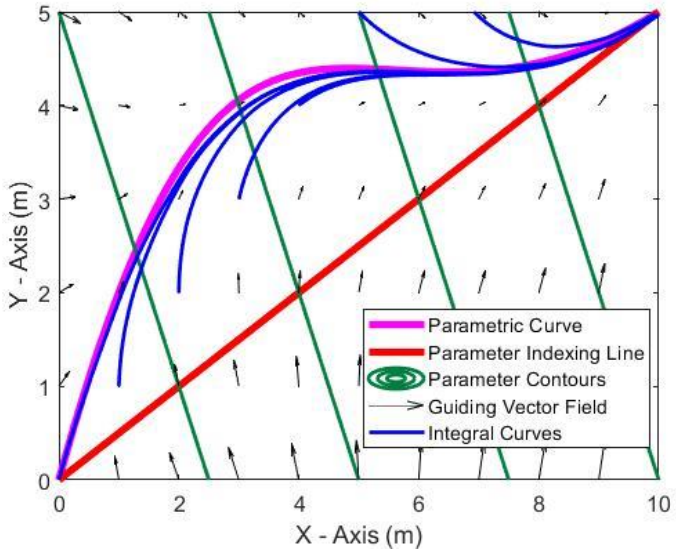

Figure 4.7 A Bézier Curve with the Modified Guiding Vector Field

Based on the scalars in (4.36), the curve parameter in (4.37) takes admissible values in the set $S = \{(x, y) \in \mathbb{R}^2 : 0 \leq \alpha(x, y) \leq 25\}$. Therefore, if a vehicle is restricted to lie in this set, the integral curves of the modified guiding vector field would flow towards the reference path. This is reflected by the integral curves in Figure 4.7.

4.5.6 Applicability of the Modified Guiding Vector Field

It was mentioned in section 4.5.5 that the integral curves of the modified guiding vector field are asymptotically stable indicating that if a vehicle is initially positioned anywhere between the endpoints of the reference path, it can smoothly merge onto the reference path. We remark that the direction of the vector field is influenced by the choice of endpoints assigned to C_0 and C_1 in (4.12). In the Bézier curve example, if the scalars C_0 and C_1 were reversed in (4.36), then the vector field and the integral curves in Figure 4.7 would be directed towards the opposite endpoint. Thus, the direction of travel dictated by the algorithm can easily be reversed by switching the constants C_0 and C_1.

In some cases, it may be impossible for the modified guiding vector field to cover an entire reference path. Let $\lambda, \gamma \in I \subset \mathbb{R}$ be two arbitrarily distinct curve parameter values. The modified vector field covers an entire reference path if condition (4.38) is satisfied.

$$\max(\|r_c(\lambda) - r_c(\gamma)\|_2) = \|(r_c(\beta_1) - r_c(\beta_0)\|_2 \tag{4.38}$$

Alternatively, (4.38) states the endpoints of the reference path must be the furthest points apart on the curve. This condition is implied by the domain of (4.13), which is dictated by the length of the PIL. If condition (4.38) is not satisfied for a parametric function, then S covers only a portion of that reference path (Figure 4.8) and therefore the algorithm would be partially applicable. One may argue a solution to this problem would be to partition a reference path into a number of smaller curves with at least C^1 continuity between the segments and then apply the algorithm to each segment (Figure 4.9). However, each curve segment will have its own domain set, S_i and $\bigcap_{i=1}^{n} S_i \neq \emptyset$. If a vehicle lies within the intersection of any number of S_i, then multiple vector fields will be present simultaneously instructing a vehicle to move towards each curve segment. Although one can avoid this situation by applying the algorithm when a vehicle lies outside the intersections, the applicable domain with multiple curve segments becomes more restrictive that of a single curve and there is no guarantee a vehicle would be able to converge to a reference path. This was not an issue for the roundabout path from figure 4.4 because each of the path segments satisfied condition (4.38).

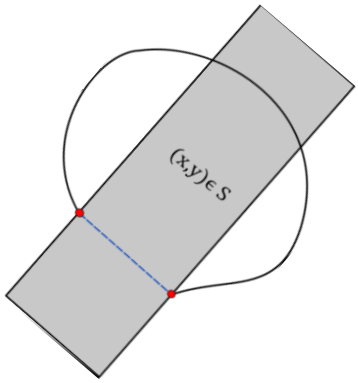

Figure 4.8 Limitation of the Modified Guiding Vector Field

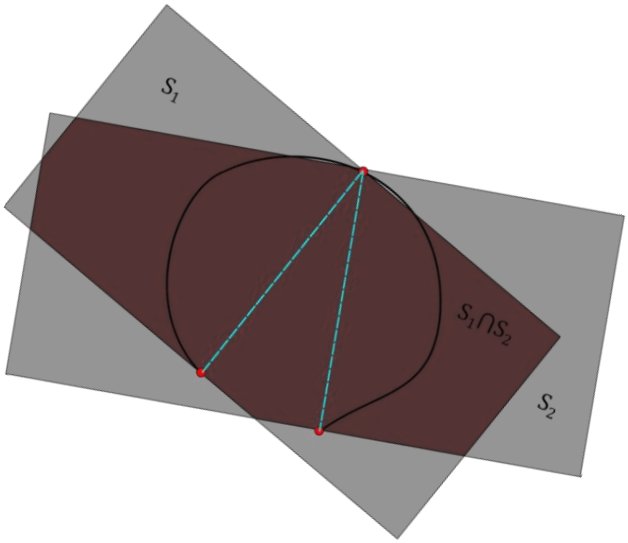

Figure 4.9 The Conflict Caused by Overlapping Modified Guiding Vector Fields

4.6 Actuator Control

The velocity commands, from the modified guiding vector field, cannot actuate the Prius to perform the path following task because they are not physically controllable inputs. Therefore, an actuator controller is needed to convert the velocity commands into physical inputs for the Prius. The inputs required to move the Prius would be those that can steer, accelerate, and brake the vehicle. One approach would be to map the velocity commands into pedal and

steering wheel commands, however there are no explicit relationships between them. Therefore, we assume the front wheels of the Prius can be actuated independently by torque commands. The front wheels were chosen because the Prius is front wheel driven and explicit relationships were found that relate velocity commands to the wheel torques.

Consider the planar vehicle model in figure 4.10

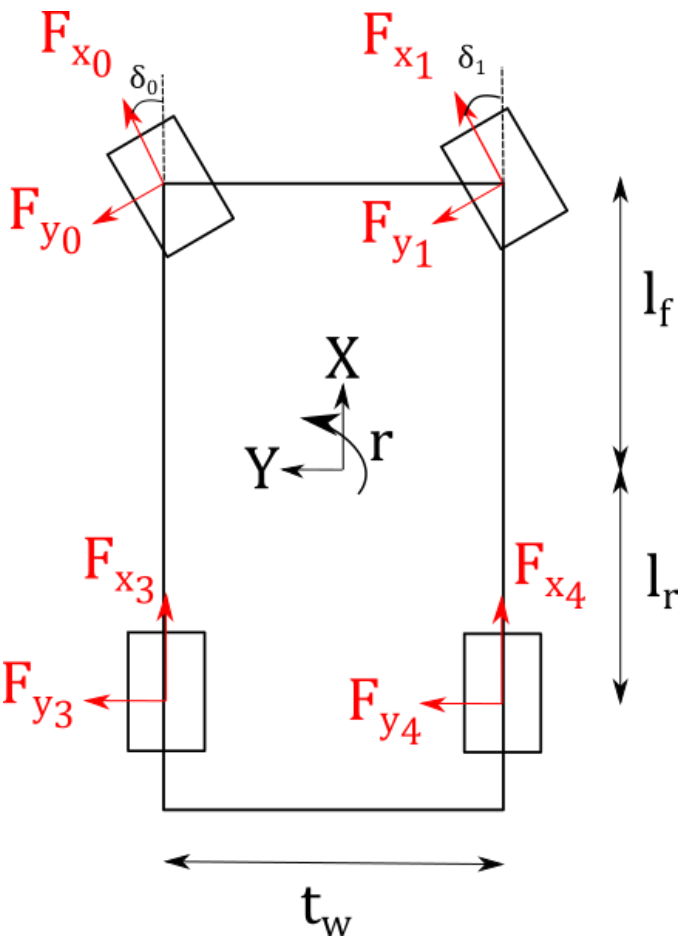

Figure 4.10 Planar Vehicle Model

Based on this model the resultant forces and yaw moment of the vehicle can be expressed as

$$
\begin{aligned}
F_X &= \left(F_{x_0}\cos(\delta_0) + F_{x_1}\cos(\delta_1) + F_{x_3} + F_{x_4}\right) \\
&- \left(F_{y_0}\sin(\delta_0) + F_{y_1}\sin(\delta_1) + F_{y_3} + F_{y_4}\right) \\
F_Y &= \left(F_{x_0}\sin(\delta_0) + F_{x_1}\sin(\delta_1) + F_{x_3} + F_{x_4}\right) \\
&+ \left(F_{y_0}\cos(\delta_0) + F_{y_1}\cos(\delta_1) + F_{y_3} + F_{y_4}\right) \\
M_Z &= \frac{t_w}{2}\left(F_{x_1}\cos(\delta_1) - F_{y_1}\sin(\delta_1) - F_{x_0}\cos(\delta_0) + F_{y_0}\sin(\delta_0) + F_{x_4} - F_{y_4}\right. \\
&\left. - \mathrm{F}_{\mathrm{x}_3} + F_{y_3}\right) \\
&+ l_f\left(F_{x_0}\sin(\delta_0) + F_{y_0}\cos(\delta_0) + F_{x_1}\sin(\delta_1) + F_{y_1}\sin(\delta_1)\right) \\
&- l_r(F_{x_3} + F_{y_3} + F_{x_4} + F_{y_4})
\end{aligned}
\tag{4.39}
$$

Where the F_{x_i} are the longitudinal tire forces, F_{y_i} are the lateral tire forces and the δ_i are the steering angles of the front wheels. The index, i refers to the wheels as referenced in figure 4.10. The parameters t_w, l_f and l_r are the trackwidth, and the distances between the Prius' center of mass and the axles, respectively. Where f is the front axle and r is the rear axle.

Using (4.39), one can derive the following state space model for the vehicle's velocity based on Newton's Second Law. It was assumed the vehicle would travel at a constant longitudinal velocity when deriving this relationship.

$$
\begin{bmatrix} \dot{v}_x \\ \dot{v}_y \\ \dot{r} \end{bmatrix} = \begin{bmatrix} -v_y r \\ v_x r \\ 0 \end{bmatrix} + \begin{bmatrix} \frac{1}{m} & 0 & 0 \\ 0 & \frac{1}{m} & 0 \\ 0 & 0 & \frac{1}{I_Z} \end{bmatrix} \begin{bmatrix} F_X \\ F_Y \\ M_Z \end{bmatrix} \tag{4.40}
$$

In (4.40), the mass of the Prius is represented by m and the yaw moment of inertia of the Prius is represented by I_Z. One may argue that substituting (4.39) into (4.40) may be better suited for actuator control design because this would incite a direct relationship between a vehicle's velocity and our desired inputs. However, the resulting state space model would pose

two challenges affecting its usability. Firstly, the state space model would be nonaffine with respect to the inputs. Most literature on controlling nonlinear systems are limited to systems which are affine in the control inputs. Among literature devoted to controlling nonaffine systems, the nonaffine systems considered are usually restricted to a class of nonaffine systems [108, 109, 110]. Furthermore, neural network approaches are commonly used for nonaffine systems Secondly, the relationship between the accelerations, steering angles and longitudinal tire forces are not injective. That is, a controller designed with a direct relationship would not assign unique pairs of longitudinal tire forces and steering angles. Therefore, by declaring the expressions on the right-hand side to be the control inputs: $F = [F_X, F_Y, M_Z]^T$ we can establish control affinity.

The resultant forces and resultant yaw moment can be computed as control inputs for a tracking problem where the reference signal comes from the modified guiding vector field through expressions (4.20) and (4.21). The state space model in (4.40) was reformulated in terms of the error dynamics, as shown in (4.41), and a combination of feedback linearization and linear quadratic regulation were used to determine the control inputs. It was assumed that the error dynamics in 4.41 were controllable and observable.

$$\begin{bmatrix} \dot{e_x} \\ \dot{e_y} \\ \dot{e_r} \end{bmatrix} = \begin{bmatrix} -e_y e_r + r_{ref} e_y + y_{ref} e_r \\ e_x e_r - r_{ref} e_x - v_{x_{ref}} e_r \\ 0 \end{bmatrix} + \begin{bmatrix} v_{y_{ref}} r_{ref} \\ -v_{x_{ref}} r_{ref} \\ 0 \end{bmatrix} + \begin{bmatrix} \frac{1}{m} & 0 & 0 \\ 0 & \frac{1}{m} & 0 \\ 0 & 0 & \frac{1}{I_Z} \end{bmatrix} \begin{bmatrix} F_X \\ F_Y \\ M_Z \end{bmatrix} \quad (4.41)$$

The terms e_x, e_y and e_r refer to the velocity errors from the system in (4.40) and the reference velocities are referred to by the subscript *ref*. These reference velocities come from the modified guiding vector field. The chosen physical inputs that would drive the vehicle were wheel torques at the front wheels and the steering angles at the wheels. Other tire forces were assumed to be known so they were treated as external inputs. The front wheels were chosen because the Prius is front wheel driven. To determine the tire force and steering angle inputs from the state space model (4.41), an approach inspired by tire force distribution algorithms

was used where an online optimization process was formulated [111, 112, 113]. We wanted to identify tire forces and a steering angle that minimized the cost function.

$$J = \int_0^t \left(\hat{F}_X(Q_x, \delta) - F_X\right)^2 + \left(\hat{F}_Y(Q_x, \delta) - F_Y\right)^2 + \left(\widehat{M_Z}(Q_x, \delta) - M_Z\right)^2 dt \qquad (4.42)$$

This cost function represents a least squares optimization problem. We compute the resultant forces and moments by computing the resultant forces in (4.39) using the determined longitudinal tire forces and steering angles. The outputs of these values are represented by $\hat{F}_X, \hat{F}_Y$ and $\widehat{M}_Z$ respectively. The input variables, Q_x and δ are vectors with component representation: $Q_x = \left[F_{x_0}, F_{x_1}\right]^T$ and $\delta = [\delta_0, \delta_1]^T$.

$$\left(\frac{Q_i}{\mu_x F_{z_i}}\right)^2 + \left(\frac{F_{y_i}}{\mu_y F_{z_i}}\right)^2 < 1$$
$$\cot \delta_{\text{out}} - \cot \delta_{in} = \frac{t_f}{l_f + l_r} \qquad (4.43)$$

The goal of the optimization problem was to determine wheel torques and a steering angle such that the resultant forces and resultant moment from the computed wheel torques and steering angle match closely with the resultant forces and resultant yaw moment from the upper level controller. The constraints from (4.43) were motivated by the requirement for vehicle maneuverability. The first constraint stems from the friction ellipse concept in section 3. By enforcing this constraint, the wheel torques computed by the optimization algorithm would be within the adhesion region. This ensures that the wheel torques are in a safe zone where the vehicle can steer and respond accordingly. The added conservatism by the friction ellipse further reinforces confidence that the longitudinal tire forces would be far from the sliding region [86]. The second constraint comes from the Ackermann steering condition [113, 14]. The Ackermann steering condition comes from geometrically modelling the kinematics of a turn. It ensures that the front tires roll while incurring the least amount of lateral slip while turning. In the optimization algorithm, this prevents excessive lateral forces from developing. To apply the steering condition from (4.43), the sign of the resultant lateral forces were considered. Using this fact, appropriate switches can be made to the inner and outer steering

angles for evaluation of the steering constraint. Once the longitudinal tire forces are determined by the optimization algorithm, they were multiplied by the effective rolling radius of the tire to compute the required wheel torque. The wheel torques are then passed as inputs to the corresponding wheels of the high fidelity model. The online optimization process was implemented into a MATLAB code using the *fmincon* function [97].

It was found that using the optimization algorithm to simultaneously determine wheel torques and steering angles was quite computationally demanding and impractical. To reduce computation time, the steering angle was removed as a design variable from the optimization process and was treated as an external parameter that would be computed by an external algorithm. Using the Stanley method [114], an appropriate steering angle could be computed based on the cross-track error of the vehicle from the path so that the vehicle is steered towards the path. The Stanley method was designed to reduce cross-track errors and it takes vehicle speeds into consideration. This makes the Stanley method suitable for path following. With the steering angle becoming an external parameter the second constraint in (4.43) was replaced with

$$\begin{cases} F_{x_0} > F_{x_1}, & if\ \delta > 0 \\ F_{x_0} < F_{x_1}, & if\ \delta < 0 \end{cases} \tag{26}$$

This constraint ensures that one of the longitudinal tire forces will be larger than the other to enforce turning. The constraint was motivated by the fact that when a vehicle turns, one of the longitudinal tire forces will be larger than the other because the outer wheel of a vehicle travels a larger distance. The condition depends on whether the Prius is turning to the left or turning to the right. Introducing the steering angle as an external parameter also eliminated the injectivity problem. The optimization algorithm would be directed to unique wheel torque values due to a predefined steering angle. Furthermore, it was found that there was a considerable reduction in computation time for the optimization algorithm. The drawback with this approach, however, was that the Ackermann condition could no longer be imposed. Therefore, the steering angles that would be computed may not necessarily cause the least

amount lateral slip. Nonetheless, after the steering angle was used by the optimization algorithm, it was passed as an argument to the front wheels of the high-fidelity model.

4.7 Path Following Results

The path following controller was applied to the upgraded high fidelity model presented in Chapter 3 and the performance of the path following controller was analyzed by plotting the cross-track error with respect to time (Figure 4.11). The corresponding path that was followed by the Prius is presented in Figure 4.13. The cross-track error was an appropriate measure of controller performance because it indicated how far away the center of mass of the Prius was with respect to the reference path. Figure 4.12 shows the longitudinal velocity of the Prius model as it traverses the path. The vehicle was given an initial velocity of 3m/s and was positioned at the left end of the roundabout.

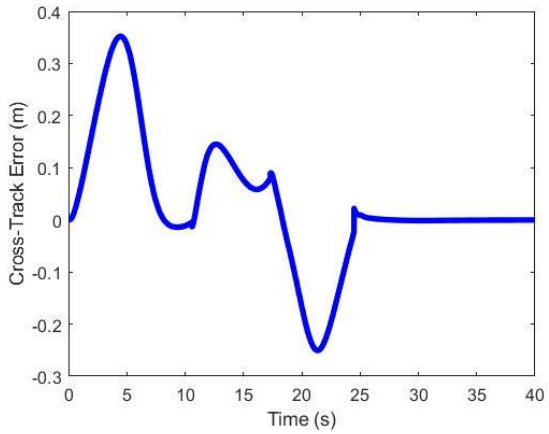

Figure 4.11 Plot of Cross-Track Error Over Time

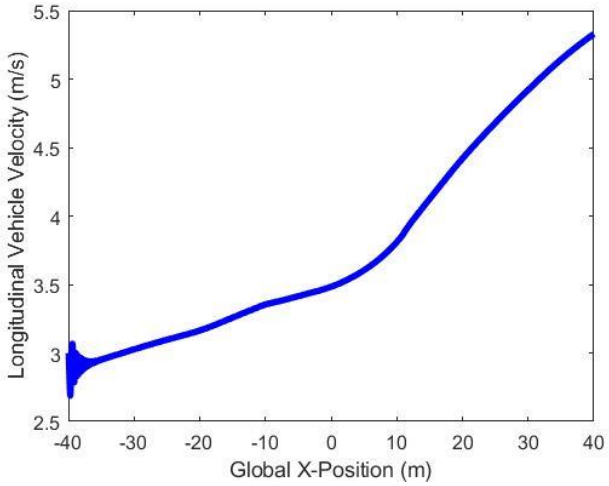

Figure 4.12 Longitudinal Velocity of High-Fidelity Model

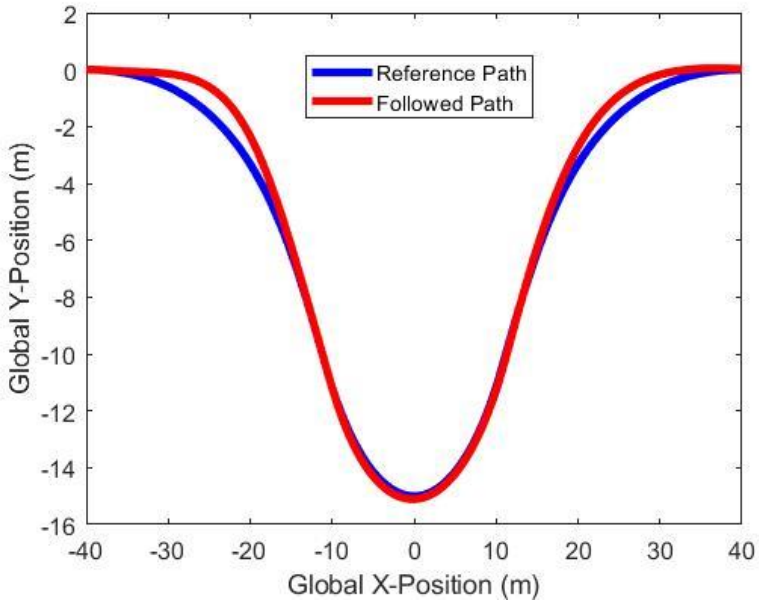

Figure 4.13 Followed Path versus Reference Path

According to Figure 4.11, the cross-track error decreased while the Prius was tasked to traverse each curve segment. This agreed with the stability result that was produced in section 4.3.3. However, the Prius showed a tendency to deviate away from the reference path upon

entering and exiting the path. The appearance of the deviation shows that the vehicle is not steering enough when turning. This indicates an understeer characteristic [14] because the vehicle is accelerating according to Figure 4.12. Understeer is a phenomenon associated with vehicle turning where a vehicle exhibits less turning effort than commanded because it is accelerating. Physically, understeering is usually caused by slip angles of the front tires being larger than that of the rear tires. Wong explains if a vehicle is accelerating while turning, greater steering angles are required to negotiate a turn [14]. The Stanley Method relies on a tunable parameter that influences the steering angle based on a vehicle's speed [114]. If correctly tuned, the vehicle may show better alignment with the reference path when entering and exiting roundabouts. Consequently, this would reduce the maximum deviation from the reference path. Currently, the maximum deviation is about 0.35m (Figure 4.11) which may be unsafe for roundabout entry.

Figure 4.12 reveals the vehicle accelerated as it traversed the roundabout. This is a favorable response considering that drivers accelerate their vehicles while traversing roundabouts [13]. Additionally, the vehicle had a greater acceleration as it was leaving the roundabout. Compared to the findings by Zhao et al., this result shows a path following approach encourages autonomous vehicles to be bolder than human drivers when traversing roundabouts. However, this could be caused by the unconstrained structure of the path. There were no obstacles or lanes thereby granting greater freedom for the Prius model. Despite the accelerations, the maximum velocity was roughly 5.5m/s (19.8km/h) which is close to the speeds observed by Zhao et al. for drivers in a roundabout [13].

Figures 4.14 to 4.16 show snapshots of the high fidelity model on the entry curve, roundabout circle and the exit path. They indicate that the high fidelity model was appropriately oriented when traversing the reference path.

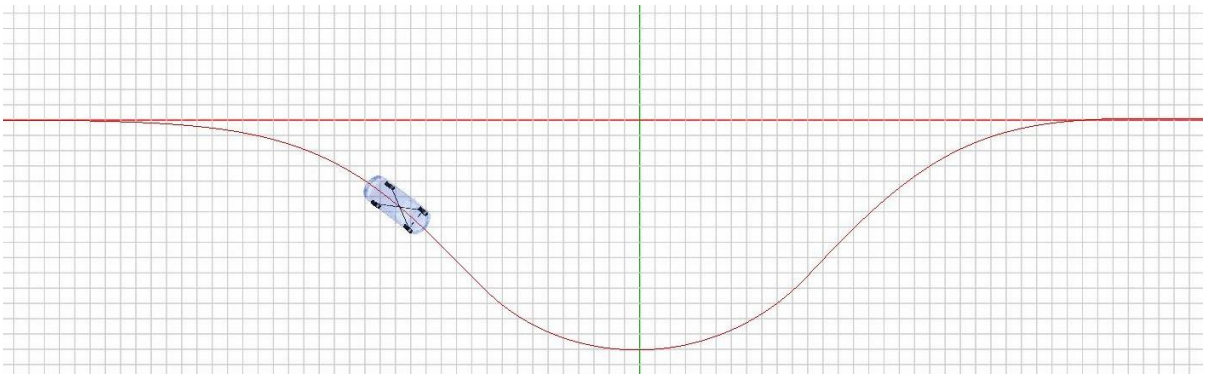

Figure 4.14 High Fidelity Model on the Entry Path

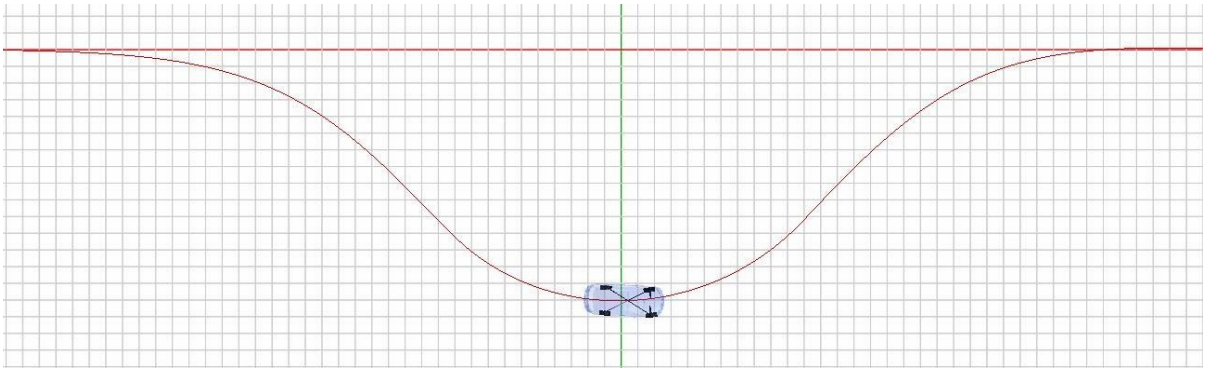

Figure 4.15 High Fidelity Model Traversing the Roundabout Circle

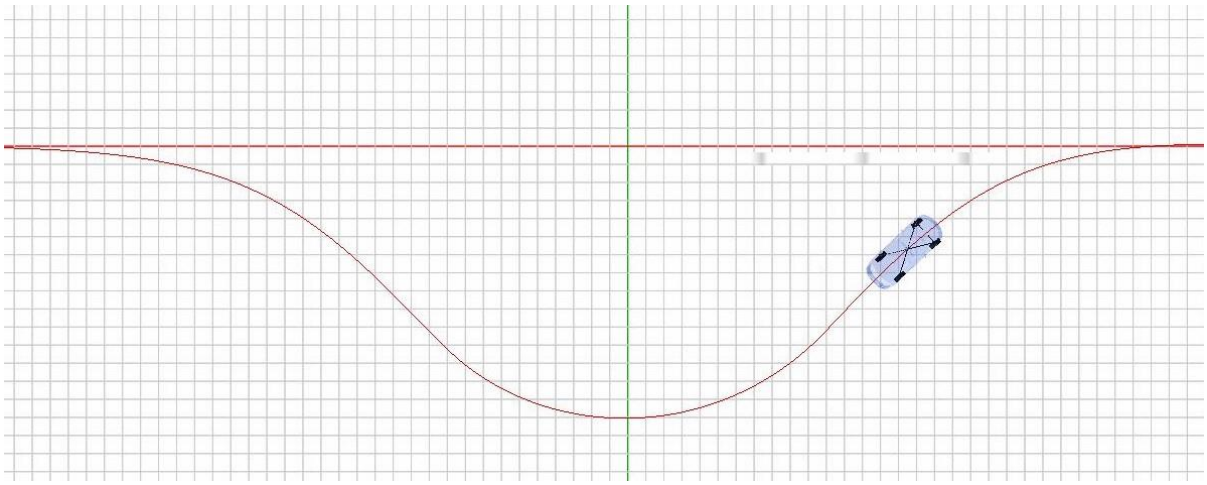

Figure 4.16 High Fidelity Model on the Exit Path

The path following controller presented is shown to be capable of allowing vehicles to closely follow paths for roundabout navigation. However, this control architecture does not control speed very well. Yet, accelerating a vehicle on a roundabout is natural for drivers [13]. In spite of this, the path following controller performs well since the high fidelity model shows little deviation from the reference path.

Chapter 5
Conclusions and Future Work

5.1 Conclusions

With respect to vehicle dynamics modelling, this work presented the challenges and complexities of accurately capturing turning motion. Two of these challenges were tire modelling and suspension K&C.

In considering general vehicle turning behaviors, commonly used pure slip tire force models are no longer sufficient. Turning vehicles often accelerate or decelerate which profoundly influences tire forces during a turn. Pure slip tire models become insufficient cannot characterize these changes. Combined slip tire models, however, can better represent tire forces during general turning maneuvers. Although various combined slip tire force models in literature were classified as accurate, this work revealed the accuracy of these tire models significantly differed when compared to driving data. Driving introduces additional effects that challenge the accuracy of combined slip tire models. Additionally, this work demonstrated the need to compare combined slip tire force models with respect to driving data. Doing so, alleviates doubt when selecting combined slip tire models for application. The comparison of combined slip tire force models in this work revealed the State Stiffness model and the Region Invariant Slip model agreed best with the track test data. Both models originated from the Brush model indicating that this model may be a reliable resource for deriving combined slip tire force models.

Suspension (K&C) modelling is a challenging task because of the necessity for multibody representations of a suspension geometry. This adds computational and modelling effort for vehicle components with negligible inertial properties. Fortunately, the SEK joint simplifies this process. The SEK joint alleviated the issue by replacing the suspension geometry with a set of uniquely defined constraints. These constraints can be made by fitting parametric reference curves to suspension motion data. The SEK joint adds little to computational intensity and could be a considered as a preferred approach to modelling suspension K&C .

This thesis also advocated for exploration of path following strategies in autonomous vehicle navigation. Literature indicates path following offers several advantages over standard trajectory tracking methods such as robustness, reduced control effort, and mitigated transient effects. Moreover, path planning algorithms generate reference paths so path following seems like a suitable pair with these strategies. Vector field methods were shown to be the best performing path following algorithms with respect to minimizing errors. A promising algorithm for autonomous vehicle navigation from this class of methods is the GVF algorithm. However, the GVF is limited to contour map representations of reference paths. Hence, the GVF cannot be paired with path planning algorithms relying on parametric functions. Using one-forms shows that it is possible to alter the GVF algorithm so that it is applicable to parametric curves. With little added complexity, the MGVF algorithm provides favorable stability conditions to encourage its use with path planning.

5.2 Future Work

There are multiple areas of exploration to advance the modelling work presented here. Firstly, the combined slip tire force models used in the comparative study represent a small subset of the available combined slip tire force models. This comparison could be extended to more combined slip tire force models to identify models that better predict tire forces. In doing so, further vehicle tire testing may be needed to identify parameters for additional tire models. It was mentioned in section 3, that standard data processing techniques cannot be used on driving data. If driving data is used more frequently, data processing techniques that handle vertical tire load fluctuations and changes in wheel orientation would need to be developed. Furthermore, the motion of the Prius model needs to be validated with the addition of the combined slip tire force models. This can be done using data from the combined slip test mentioned in section 3. By comparing motion variables of the chassis and tires, one can gauge how consistent the model behavior is with an actual Prius.

Although an implementation of the SEK joint was presented, new suspension parameters are required for application to the Prius model. Estimating the parameters will require suspension data that could be generated by a four-post test or a speed hump drive test. To further enhance

the SEK joint suspension model, one can add compliance and steering effects. Hall presented an extension of the SEK joint to include suspension compliance and steering formulating a compliant Double Equivalent Kinematic (DEK) joint [55]. This would require changes to the K&C test presented in section 3 such that steering, and deformation of the suspension bushings is included. Implementation of this joint may require modelling bushings and estimating bushing parameters.

The path following algorithm produces wheel torques and tire steering angles to actuate a vehicle. However, a more natural approach would be to identify accelerator pedal positions, brake pedal positions and steering wheel commands. If the framework presented here is to be used, a powertrain model of the Prius, engine model and a steering system model would be required. These models would also be required for the high fidelity model for controller testing. A promising powertrain model that could be paired with the path following approach presented here is the one by Hosking [115]. Hosking presented a hybrid powertrain model based on neural networks that could allow one to assign pedal positions to wheel torques. Powertrain testing of the Prius would be required to replicate the neural network for a high fidelity model.

References

[1] S. Pendleton, H. Andersen, X. Du, X. Shen, M. Meghjani, Y. Eng, D. Rus and M. Ang Jr., "Perception, Planning, Control and Coordination for Autonomous Vehicles," *Machines,* vol. 5, no. 6, pp. 1-54, 2017.

[2] I. Barabas, A. Todorut, N. Cordos and A. Molea, "Current Challenges in Autonomous Driving," in *IOP Conference Series in Materials Science and Engineering*, 2017.

[3] J. Greenblatt and S. Shaheen, "Automated Vehicles, On-Demand Mobility and Environmental Impacts," *Current Sustainable/Renewable Energy Reports,* vol. 2, no. 3, pp. 74-81, 2015.

[4] Tesla Canada, "Tesla Autopilot," [Online]. Available: https://www.tesla.com/en_CA/autopilot.

[5] M. Askarihemmat, "Path Planning Algorithms for Autonomous Mobile Robots," Concordia University, Montreal, Canada, 2018.

[6] S. LaValle, Planning Algorithms, Cambridge University Press, 2006.

[7] D. Mayne, "Model Predictive Control: Recent Developments and Future Promise," *Automatica,* vol. 50, pp. 2967-2986, 2014.

[8] R. Elvik, "Effects on Road Safety of Converting Intersections to Roundabouts: Review of Evidence from Non-U.S. Studies," *Transportation Research Record: Journal of the Transportation Research Board,* vol. 1847, no. 1, pp. 1-10, 2003.

[9] Greater Sudbury, "Comparative Analysis: Roundabout vs. Signalled Intersection," City of Greater Sudbury, Sudbury, Canada.

[10] L. Wang, "Roundabout Safety Benefit-Cost Analysis in Nevada," University of Nevada, Nevada, USA, 2020.

[11] E. Dabbour and S. Easa, "Proposed Geometric Features to Improve the Safety of Modern Roundabouts," in *Transportation Research Board,* Washington, USA, 2006.

[12] Ontario Ministry of Transportation, "How to Use Roundabouts Brochure," 18 6 2012. [Online].

[13] M. Zhao, D. Kathner, M. Jipp, D. Soffker and K. Lemmer, "Modelling Driver Behavior at Roundabouts: Results From a Field Study," in *IEEE Intelligent Vehicles Symposium*, Los Angeles, USA, 2017.

[14] J. Wong, Theory of Ground Vehicles, Wiley, 2008.

[15] S. Buggaveeti, "Dynamic Modelling and Parameter Identification of a Plug-in Hybrid Electric Vehicle," UWSpace, 2017.

[16] B. Zhu, S. Liu and J. Zhao, "A Lane-Changing Decision-Making Method for Intelligent Vehicle Based on Acceleration Field," *SAE Technical Paper,* 2018.

[17] Y. Wang, R. Feng, D. Pan, Z. Liu, N. Wu and W. Li, "The Trajectory Planning of the Lane Change Assist Based on the Model Predictive Control with Multi-Objective," *SAE Technical Paper,* 2017.

[18] MSC Software, "ADAMS Car Brochure," 2019. [Online].

[19] Mechanical Simulation Corporation, "CarSim Brochure," [Online].

[20] MathWorks, "Simscape User's Guide," 2020. [Online].

[21] Maplesoft, "MapleSim User's Guide," 2020. [Online].

[22] J. McPhee, C. Schmitke and S. Redmond, "Dynamic Modelling of Mechatronic Multibody Systems with Symbolic Computing and Linear Graph Theory," *Mathematical and Computer Modelling of Dynamical Systems,* vol. 10, no. 1, pp. 1-23, 2004.

[23] H. B. Pacejka and I. Besselink, Tire and Vehicle Dynamics, Oxford: Butterworth-Heinemann, 2012.

[24] D. Nordeen, "Analysis of Tire Lateral Forces and Interpretation of Experimental Tire Data," *SAE Technical Paper,* pp. 969-980, 1967.

[25] A. Bhoraskar and P. Sakthivel, "A Review and a Comparison of Dugoff and Modified Dugoff with Magic Formula," in *International Conference on Nascent Technologies in the Engineering Field*, Mumbai, India, 2017.

[26] H. Dugoff, P. Fancher and L. Segel, "An Analysis of Tire Traction Properties and Their Influence on Vehicle Dynamic Performance," *SAE Technical Paper,* 1970.

[27] E. Bakker, L. Nyborg and H. Pacejka, "Tyre Modelling for Use in Vehicle Dynamic Studies," SAE International, 1987.

[28] C. Canudas de Wit and P. Tsiotras, "Dynamic Tire Friction Models for Vehicle Traction Control," in *IEEE Conference on Decision and Control*, Arizona, USA, 1999.

[29] M. Brach and R. Brach, "Modelling Combined Braking and Steering Tire Forces," SAE International, 2000.

[30] P. Bayle, J. Forissier and S. Lafon, "A New Tyre Model for Vehicle Dynamic Simulation," Automotive Technology International, 1993.

[31] E. Kuiper and J. Van Oosten, "The PAC2002 Advanced Handling Tire Model," *Vehicle System Dynamics,* vol. 45, no. Supplement, pp. 153-167, 2007.

[32] S. Taheri and T. Wei, "A New Semi-Empirical Method for Estimating Tire Combined Slip Forces," *SAE International Journal of Passenger Cars,* vol. 8, no. 2, pp. 797-815, 2015.

[33] D. Schuring, W. Pelz and M. Pottinger, "A Model for Combined Tire Cornering and Braking Forces," SAE International, 1996.

[34] N. Xu and K. Gao, "Modelling Combined Braking and Cornering Forces Based on Pure Slip Measurements," *SAE International Journal of Commerical Vehicles,* vol. 5, no. 2, pp. 470-482, 2012.

[35] M. Gafvert and J. Svendenius, "A Novel Semi-Empirical Tyre Model for Combined Slips," *Vehicle System Dynamics,* vol. 43, no. 5, pp. 351-384, 2005.

[36] M. Pottinger, W. Pelz and G. Falciola, "Effectiveness of the Slip Circle, “COMBINATOR”, Model for Combined Tire Cornering and Braking Forces When Applied to a Range of Tires," SAE International, 1998.

[37] K. Guo, D. Lu, S.-K. Chen, W. Lin and X.-P. Lu, "The UniTire model: A Nonlinear and Non-Steady-State Tyre Model for Vehicle Dynamic Simulation," *Vehicle System Dynamics,* vol. 43, no. Supplement, pp. 341-358, 2005.

[38] D. Lu and K. Guo, "UniTire: Unified Tire Model for Vehicle Dynamic Simulation," *Vehicle System Dynamics,* vol. 45, no. Supplement, pp. 79-99, 2007.

[39] N. Xu, D. Lu and S. Ran, "A Predicted Tire Model for Combined Tire Cornering and Braking Shear Forces Based on the Slip Direction," in *International Conference on Electronic & Mechanical Engineering and Information Technology*, 2011.

[40] K. Guo and J. Sui, "A Theoretical Observation on Empirical Expression of Tire Shear Forces," *Vehicle System Dynamics,* vol. 25, no. Supplement, pp. 263-274, 1996.

[41] MSC Software, "ADAMS Tire Help Manual".

[42] M. Gafvert and J. Svendenius, "A Semi-Empirical Dynamic Tire Model for Combined - Slip Forces," *Vehicle System Dynamics,* vol. 44, no. 2, pp. 189-208, 2006.

[43] M. Gafvert and J. Svendenius, "A Semi-Empirical Tire Model For Combined Slips Including the Effects of Cambering," in *3rd International Tyre Colloquium: Tyre Models For Vehicle Dynamics Analysis*, Vienna, 2004.

[44] M. Gafvert and J. Svendenius, "A Semi-Empirical Tire Model for Transient Combined-Slip Forces," in *International Symposium on Advanced Vehicle Control*, 2004.

[45] M. Van Gennip and J. McPhee, "Parameter Identifcation and Validation for Combined Slip Tire Models Using a Vehicle Measurement System," *SAE International Journal of Vehicle Dynamics, Stability and NVH,* vol. 2, no. 4, pp. 297-310, 2018.

[46] V. Nicholas and T. Comstock, "Predicting Directional Behavior of Tractor Semitrailers When Wheel Anti-Skid Braking Systems Are Used," in *ASME Winter Annual Meet*, 1972.

[47] D. Cao, X. Song and M. Ahmadian, "Road Vehicle Suspension Design, Dynamics and Control," *Vehicle System Dynamics,* vol. 49, no. 1-2, pp. 3-28, 2011.

[48] J. Reimpell, H. Stoll and J. Betzler, Automotive Chassis: Engineering Principles, Butterworth-Heinemann, 2001.

[49] T. Shim and P. Veluswamy, "Influence of Suspension Properties on Vehicle Roll Stability," in *SAE Automotive Dynamics, Stability and Controls Conference*, Novi, Michigan, 2006.

[50] J. Park and P. Nikravesh, "Effect of Steering-Housing Rubber Bushings on the Handling Responses of a Vehicle," in *SAE International Congress and Exposition*, Detroit, Michigan, 1997.

[51] M. Blundell, "The Influence of Rubber Bush Compliance on Vehicle Suspension Movement," *Materials and Design,* vol. 19, no. 1, pp. 29-37, 1998.

[52] S. Lajqi, S. Pehan, N. Lajqi, A. Gjelaj, J. Psenicnik and S. Emin, "Design of Independant Suspension Mechanism for a Terrain Vehicle with Four Wheels Drive and Four Wheels Steering," *Annals Faculty of Engineering Hunedoara - International Journal of Engineering*, pp. 101-108, 2013.

[53] H. Schuette and P. Waeltermann, "Hardware-in-the-loop Testing of Vehicle Dynamic Controllers - A Technical Survey," SAE, 2005.

[54] L. Jing, L. Wu, X. Li and Y. Zhang, "Study on Kinematic and Compliance Test of Suspension," in *IOP Conference Series: Materials Science and Engineering*, Kunming, China, 2017.

[55] A. Hall, "Formulation of a Path-Following Joint for Multibody System Dynamics," UWSpace, 2015.

[56] J. Ginsberg, Engineering Dynamics, Cambridge University Press, 2007.

[57] B. Rubi, R. Perez and B. Morcego, "A Survey of Path Following Control Strategies for UAV's Focused on Quadrotors," *Journal of Intelligent and Robotic Systems*, vol. 98, pp. 241-265, 2019.

[58] P. Sujit, S. Saripalli and J. Sousa, "Unmanned Aerial Vehicle Path Following: A survey And Analysis of Algorithms," *IEEE Control Systems Magazine*, pp. 42-59, February 2014.

[59] A. Aguiar, D. Dacic, J. Hespanha and P. Kokotovic, "Path-Following or Reference Tracking? An Answer Relaxing the Limits to Performance," in *IFAC Symposium on Intelligent Autonomous Vehicles*, 2004.

[60] A. Aguiar, J. Hespanha and P. Kokotovic, "Performance Limitations in Reference-Tracking and Path-Following for Nonlinear Systems," *Automatica*, vol. 44, no. 3, pp. 598-610, 2008.

[61] D. Dacic and P. Kokotovic, "Path Following for Linear Systems with Unstable Zero Dynamics," *Automatica*, vol. 42, pp. 1673-1683, 2006.

[62] D. Miller and R. Middleton, "On Limitations to the Achievable Path Following Performance for Linear Multivariable Plants," *IEEE Transactions on Automatic Control*, vol. 53, no. 11, pp. 2586-2601, 2008.

[63] Y. Kapitanyuk, A. Proskurnikov and M. Cao, "A Guiding Vector Field Algorithm for Path Following Control of Nonholonomic Mobile Robots," *IEEE Transactions on Control Systems Technology*, vol. 26, no. 4, pp. 1372-1385, 2017.

[64] T. Bakker, K. Asselt, J. Bontsema, J. Muller and G. Straten, "A path following algorithm for mobile robots," *Autonomous Robots*, vol. 29, pp. 85-97, 2010.

[65] D. Nelson, D. B. Barber, T. McLain and R. Beard, "Vector Field Path Following for Miniature Air Vehicles," *IEEE Transactions on Robotics*, vol. 23, no. 3, pp. 519-529, 2007.

[66] K. Do and J. Pan, "Robust Adaptive Path Following of Underactuated Ships," *Automatica*, vol. 40, no. 6, pp. 929-944, 2004.

[67] M. Breivik and T. Fossen, "Path Following for Marine Surface Vehicles," in *MTSE/IEEE Techno-Oceans '04*, Kobe, 2004.

[68] Y. Liao, M.-j. Zhang and W. Lei, "Serret-Frenet frame based on path following control for underactuated unmanned surface vehicles with dynamic uncertainties," *Journal of Central South University,* vol. 22, pp. 214-223, 2015.

[69] A. Micaelli and C. Samson, "Trajectory Tracking for Unicycle-Type and Two-Steering-Wheel Mobile Robots," INRIA, 1993.

[70] C. Samson, "Path Following and Time-Varying Feedback Stabilization of a Wheeled Mobile Robot," in *ICARCV*, Singapore, 1992.

[71] A. Micaelli, C. Samson, P. Robotique and P. Icare, "Trajectory Tracking for Unicycle-Type and Two-Steering-Wheels Mobile Robots," *IFAC Proceedings,* vol. 27, pp. 249-256, 1994.

[72] O. Amidi and C. Thorpe, "Integrated Mobile Robot Control," Carnegie Mellon University, 1991.

[73] S. Park, J. Deyst and J. How, "Performance and Lyapunov Stability of a Nonlinear Path Following Guidance Method," *Journal of Guidance Control and Dynamics,* vol. 30, pp. 1718-1728, 2007.

[74] C. Nielsen and M. Maggiore, "On Local Transverse Feedback Linearization," *SIAM Journal on Control and Optimization,* vol. 47, no. 5, pp. 2227-2250, 2008.

[75] C. Nielsen, C. Fulford and M. Maggiore, "Path Following Using Transverse Feedback Linearization: Application to a Maglev Positioning System," *Automatica,* vol. 46, pp. 585-590, 2010.

[76] L. Consolini, M. Maggiore, C. Nielsen and M. Tosques, "Path Following for the PVTOL Aircraft," *Automatica,* vol. 46, pp. 1284-1296, 2010.

[77] M. El-Hawwary and M. Maggiore, "Case Studies on Passivity-Based Stabilization of Closed Sets," *International Journal of Control,* vol. 84, no. 2, pp. 336-350, 2011.

[78] Y. Kapitanyuk, S. Chepinskiy and A. Kapitonov, "Geometric Path Following Control of a Rigid Body Based on the Stabilization of Sets," in *IFAC World Congress*, Cape Town, 2014.

[79] D. Lawrence, E. Frew and W. Pisano, "Lyapunov Vector Fields for Autonomous Unmanned Aircraft Flight Control," *Journal of Guidance, Control and Dynamics,* vol. 31, no. 5, pp. 1220-1229, 2008.

[80] W. Yajing, W. Xiangke, Z. Shulong and S. Lincheng, "Vector Field Based Sliding Mode Control of Curved Path for Miniature Unmanned Aerial Vehicles in Wind," *Journal of System Science and Complexity,* vol. 31, pp. 302-324, 2018.

[81] Y. Liang and Y. Jia, "Combined Vector Field Approach for 2D and 3D Arbitrarily Twice Differentiable Curved Path Following with UAV Constraints," *Journal of Intelligent Robotic Systems,* vol. 83, pp. 133-160, 2016.

[82] A&D Technology, "Vehicle Measurement System (VMS)," [Online].

[83] S. International, "Vehicle Dynamics Terminology". Patent J670.

[84] Racelogic, "VBox 3i," [Online]. Available: https://www.vboxautomotive.co.uk/index.php/en/products/data-loggers/vbox-3i.

[85] GKS-Perfekt, "RL1 Rotating Dolly," GKS-Perfekt, [Online]. Available: https://www.gksweb.com/rotating-dollies/rotating-dollies/rl1.html.

[86] R. Brach and B. Matthew, "The Tire - Force Ellipse (Friction Ellipse) and Tire Characteristics," SAE International, 2011.

[87] M. Gafvert and J. Svendenius, "Construction of Novel Semi-Empirical Tire Models for Combined Braking and Cornering," Lund Institute of Technology, 2003.

[88] R. Woods, "Normalization of the Pacejka Tire Model," in *SAE Motorsports Engineering Conference and Exhibition*, Dearborn, Michigan, 2004.

[89] H. Radt, "Processing of Tire Force/Moment Data," in *SAE International Congress and Exhibition*, Detroit, Michigan, 1995.

[90] C. de Boor, A Practical Guide to Splines, Springer, 1978.

[91] T. Tao and A. Watson, "An Adaptive Algorithm for Fitting with Splines," *AIChE Journal*, vol. 34, no. 10, pp. 1722-1725, 1988.

[92] M. Van Gennip, "Vehicle Dynamic Modelling and Parameter Identification for an Autonomous Vehicle," UWSpace, 2018.

[93] L. Schumaker, Spline Functions: Basic Theory, Wiley, 1981.

[94] D. Gonzalez, J. Perez and V. Milanes, "Parametric Based Path Generation for Automated Vehicles at Roundabouts," *IEEE Transactions on Intelligent Transportation Systems*, vol. 17, no. 2, 2016.

[95] D. Gonzalez, J. Perez, V. Milanes and F. Nashashibi, "A Review of Motion Planning Techniques for Automated Vehicles," *IEEE Transactions on Intelligent Transportation Systems*, vol. 17, no. 4, 2016.

[96] R. Bartels, J. Beatty and B. Barsky, An Introduction to Splines for Use in Computer Graphics and Geometric Modeling, Morgan Kaufmann, 1995.

[97] MathWorks, "MATLAB," 2020.

[98] Y. Kapitanyuk, H. de Marina, A. Proskurnikov and M. Cao, "Guiding Vector Field Algorithm for Moving Path Problem," *IFAC-PapersOnLine*, vol. 50, no. 1, pp. 6983-6988, 2017.

[99] I.-A. Ihle, M. Arcak and T. Fossen, "Passivity-Based Designs for Synchronized Path-Following," *Automatica*, vol. 43, pp. 1508-1518, 2007.

[100] R. Skjetne, T. Fossen and P. Kokotovic, "Robust Output Maneuvering for a Class of Nonlinear Systems," *Automatica*, vol. 40, pp. 373-383, 2004.

[101] J. Wang, Y. Kapitaniyuk, S. Chepinsky, D. Liu and A. Krasnov, "Geometric Path Following Control in a Moving Frame," *IFAC-PapersOnLine*, vol. 48, no. 11, pp. 150-155, 2015.

[102] H. Yamaguchi, M. Mori and A. Kawakami, "A Path Following Feedback Control Method Using Parametric Curves for a Cooperative Transportation System with Two Car-like Mobile Robots," *IFAC Proceedings,* vol. 43, no. 16, pp. 163-168, 2010.

[103] N. Loehr, Advanced Linear Algebra, CRC Press, 2014.

[104] P. Renteln, Manifolds, Tensors and Forms: An Introduction for Mathematicians and Physicists, Cambridge University Press, 2014.

[105] J. P. Fortney, A Visual Introduction to Differential Forms and Calculus on Manifolds, Birkhauser, 2018.

[106] R. Bishop and S. Goldberg, Tensor Analysis on Manifolds, Dover Publishing, 1968.

[107] J. Slotine and W. Li, Applied Nonlinear Control, Pearson, 1990.

[108] T. Binazadeh and M. Rahgoshay, "Robust output tracking of a class of non-affine systems," *System Science and Control Engineering,* vol. 5, no. 1, pp. 426-433, 2017.

[109] P. Chen, Y. Liu and G. Wen, "Fuzzy Neural Network-Based Adaptive Control for a Class of Uncertain Nonlinear Stochastic Systems," *IEEE Transactions on Cybernetics,* vol. 44, no. 5, pp. 583-593, 2014.

[110] M. Chen and S. Ge, "Direct Adaptive Neural Control for a Class of Uncertain Nonaffine Nonlinear Systems Based on Disturbance Observer," *IEEE Transactions on Cybernetics,* vol. 43, no. 4, pp. 1213-1225, 2013.

[111] H. Zheng and S. Yang, "A Trajectory Tracking Control Strategy of 4WIS/4WID Electric Vehicle with Adaptation of Driving Conditions," *Applied Sciences,* vol. 9, no. 168, 2019.

[112] B. Li, H. Du and W. Li, "Optimal Distribution Control of Non-Linear Tire Force of Electric Vehicles with In-Wheel Motors," *Asian Journal of Control,* vol. 18, no. 1, pp. 69-88, 2016.

[113] C. Wang, S. Cheng, T. Hsiao and W. Chou, "Application of Optimum Tire Force Distribution to Vehicle Motion Control," in *IEEE/ASME International Conference on Advanced Intelligent Mechatronics*, 2012, 2012.

[114] J. Snider, "Automatic Steering Methods for Autonomous Automobile Path Tracking," Carnegie Mellon University, Pittsburgh, USA, 2009.

[115] B. Hosking, "Modelling and Model Predictive Control of Power-Split Hybrid Powertrains for Self-Driving Vehicles," UWSpace, Waterloo, Canada, 2018.

[116] T. Fossen and K. Pettersen, "On Uniform Global Exponential Stability (USGES) of Proportional Line-of-Sight Guidance Laws," *Automatica,* vol. 50, pp. 2912-2917, 2014.

[117] J. Dixon, Suspension Geometry and Computation, Wiley, 2009.

[118] M. Czechowicz and G. Mavros, "Analysis of Vehicle Rollover Dynamics Using a High Fidelity Model," *Vehicle System Dynamics,* vol. 52, no. 5, pp. 608-636, 2014.

Appendix A

Prius High-Fidelity Model

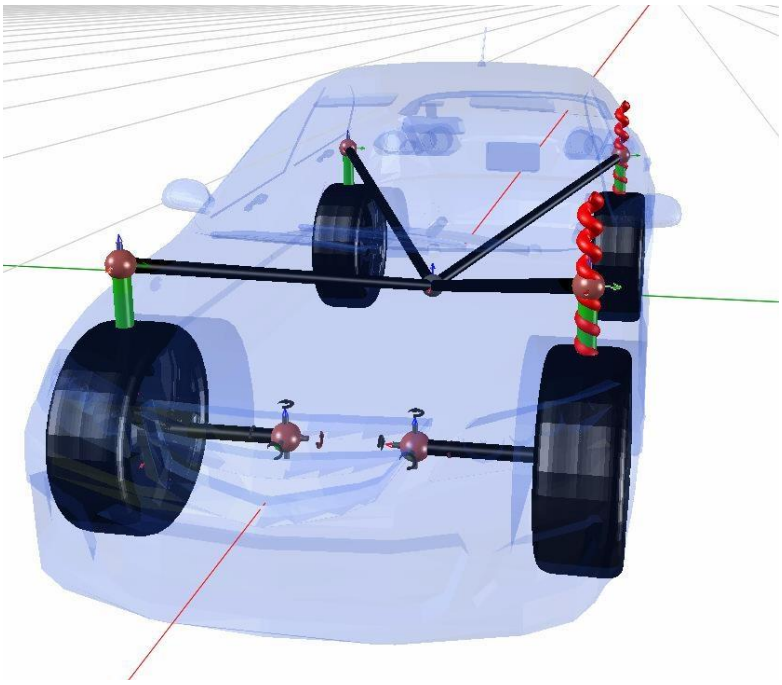

Figure A.5.1 Prius High Fidelity Model (Visual)

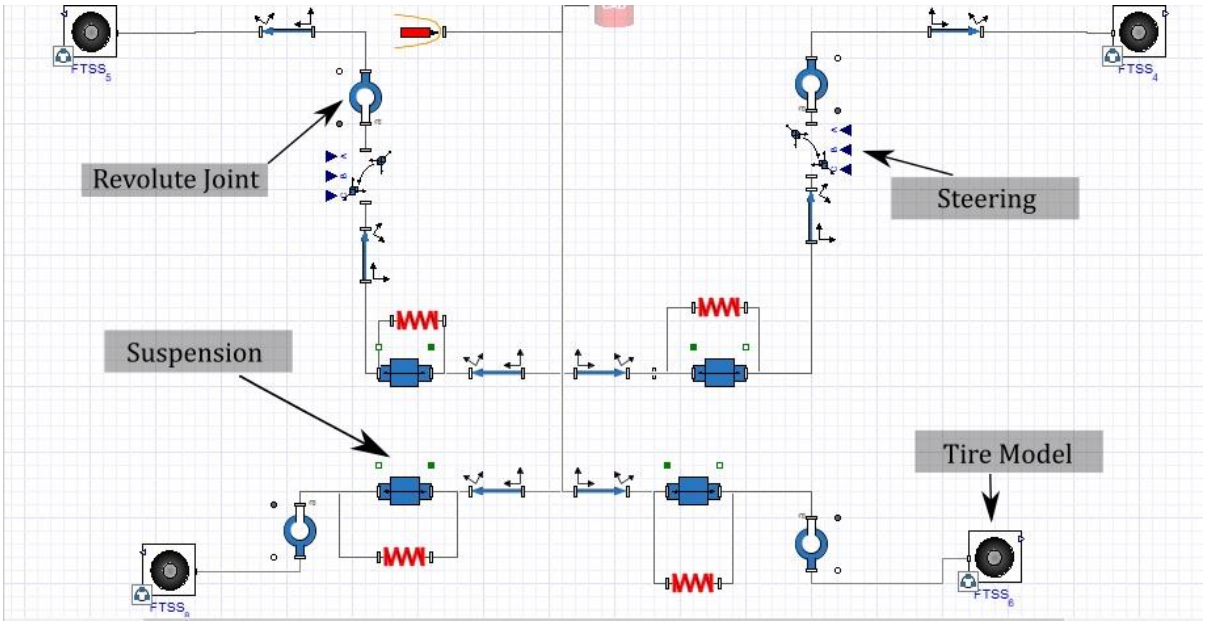

Figure A.5.2 Prius High Fidelity Model (Skeleton)

Table A.1 Prius High Fidelity Model Parameters

Vehicle Parameter	Description	Value
m	Vehicle Mass	2044 kg
L	Wheelbase	2.70 m
t_w	Trackwidth	1.72 m
l_f	Distance from Vehicle C.G. to Front Axle	1.24 m
l_r	Distance from Vehicle C.G. to Rear Axle	1.46 m
I_x	Roll Moment of Inertia	828 $kg\ m^2$
I_y	Pitch Moment of Inertia	2888 $kg\ m^2$
I_z	Yaw Moment of Inertia	2828 $kg\ m^2$
h_{CG}	Height of Center of Mass From Ground	0.6 m
m_w	Wheel Mass	17 kg
I_{w_x}	Wheel Moment of Inertia About SAE X-Axis	0.78 $kg\ m^2$
I_{w_y}	Wheel Moment of Inertia About SAE Y-Axis	1.56 $kg\ m^2$
I_{w_z}	Wheel Moment of Inertia About SAE Z-Axis	0.78 $kg\ m^2$

K_t	Tire Stiffness	$450\ ^{kN}/_{m}$
C_t	Tire Damping Coefficient	$0.5\ ^{kNs}/_{m}$
K_{fr}	Front Right Suspension Stiffness	$48.2\ kN/m$
K_{fl}	Front Left Suspension Stiffness	$48.2\ kN/m$
K_{rl}	Rear Left Suspension Stiffness	$48.2\ kN/m$
K_{rr}	Rear Right Suspension Stiffness	$48.2\ kN/m$
C_{fr}	Front Right Damping Coefficient	$0.3075\ ^{kNs}/_{m}$
C_{fl}	Front Left Damping Coefficient	$0.3075\ ^{kNs}/_{m}$
C_{rl}	Rear Left Damping Coefficient	$0.3075\ ^{kNs}/_{m}$
C_{rr}	Rear Right Damping Coefficient	$0.3075\ ^{kNs}/_{m}$

Appendix B

Tire Model Parameters

Table B.2 Magic Formula Parameters

Parameter	Description	Value
B_x	Stiffness Factor (Longitudinal)	32.99
C_x	Shape Factor (Longitudinal)	0.5485
D_x	Peak Factor (Longitudinal)	0.5431
E_x	Curvature Factor (Longitudinal)	0.7434
B_y	Stiffness Factor (Lateral)	11.79
C_y	Shape Factor (Lateral)	1.850
D_y	Peak Factor (Lateral)	0.5800
E_y	Curvature Factor (Lateral)	-5.600

Table B.3 Region Invariant Slip Parameters

Parameter	Description	Value
σ_x°	Limit Slip (Longitudinal)	0.06
σ_y°	Limit Slip (Lateral)	0.5485
ρ	Friction Coefficient Ratio	1.477